Monthly Notices of the ROYAL ASTRONOMICAL SOCIETY

MNRAS **499,** 1918–1936 (2020) doi:10.1093/mnras/staa2801
Advance Access publication 2020 September 14

The R136 star cluster dissected with *Hubble Space Telescope*/STIS – II. Physical properties of the most massive stars in R136

Joachim M. Bestenlehner [1]★ Paul A. Crowther,[1] Saida M. Caballero-Nieves [1,2] Fabian R. N. Schneider [3,4] Sergio Simón-Díaz,[5,6] Sarah A. Brands,[7] Alex de Koter,[7,8] Götz Gräfener,[9] Artemio Herrero,[5,6] Norbert Langer,[9] Daniel J. Lennon,[5,6] Jesus Maíz Apellániz [10] Joachim Puls[11] and Jorick S. Vink[12]

[1]*Department of Physics & Astronomy, University of Sheffield, Hounsfield Road, Sheffield S3 7RH, UK*
[2]*Department of Aerospace, Physics and Space Sciences, Florida Institute of Technology, 150 W. University Boulevard, Melbourne, FL 32901, USA*
[3]*Astronomisches Rechen-Institut, Zentrum für Astronomie der Universität Heidelberg, Mönchhofstr. 12-14, D-69120 Heidelberg, Germany*
[4]*Heidelberger Institut für Theoretische Studien, Schloss-Wolfsbrunnenweg 35, D-69118 Heidelberg, Germany*
[5]*Instituto de Astrofísica de Canarias, E-38200 La Laguna, Tenerife, Spain*
[6]*Departamento de Astrofísica, Universidad de La Laguna, E-38205 La Laguna, Tenerife, Spain*
[7]*Anton Pannenkoek Institute for Astronomy, University of Amsterdam, NL-1090 GE Amsterdam, the Netherlands*
[8]*Institute of Astrophysics, KU Leuven, Celestijnenlaan 200D, B-3001 Leuven, Belgium*
[9]*Argelander-Institut für Astronomie der Universität Bonn, Auf dem Hügel 71, D-53121 Bonn, Germany*
[10]*Centro de Astrobiología, CSIC-INTA, Campus ESAC, Camino bajo del castillo s/n, E-28 692 Villanueva de la Cañada, Madrid, Spain*
[11]*LMU Munich, Universitäts-Sternwarte, Scheinerstrasse 1, D-81679 München, Germany*
[12]*Armagh Observatory and Planetarium, College Hill, Armagh BT61 9DG, UK*

Accepted 2020 September 8. Received 2020 September 7; in original form 2020 July 1

ABSTRACT

We present an optical analysis of 55 members of R136, the central cluster in the Tarantula Nebula of the Large Magellanic Cloud. Our sample was observed with STIS aboard the *Hubble Space Telescope*, is complete down to about 40 $M_\odot$, and includes seven very massive stars with masses over 100 $M_\odot$. We performed a spectroscopic analysis to derive their physical properties. Using evolutionary models, we find that the initial mass function of massive stars in R136 is suggestive of being top-heavy with a power-law exponent $\gamma \approx 2 \pm 0.3$, but steeper exponents cannot be excluded. The age of R136 lies between 1 and 2 Myr with a median age of around 1.6 Myr. Stars more luminous than $\log L/L_\odot = 6.3$ are helium enriched and their evolution is dominated by mass-loss, but rotational mixing or some other form of mixing could be still required to explain the helium composition at the surface. Stars more massive than 40 $M_\odot$ have larger spectroscopic than evolutionary masses. The slope of the wind–luminosity relation assuming unclumped stellar winds is 2.41 ± 0.13 which is steeper than usually obtained (∼1.8). The ionizing ($\log Q_0$ [ph/s] = 51.4) and mechanical ($\log L_{SW}$ [erg/s] = 39.1) output of R136 is dominated by the most massive stars (> 100 $M_\odot$). R136 contributes around a quarter of the ionizing flux and around a fifth of the mechanical feedback to the overall budget of the Tarantula Nebula. For a census of massive stars of the Tarantula Nebula region, we combined our results with the VLT-FLAMES Tarantula Survey plus other spectroscopic studies. We observe a lack of evolved Wolf–Rayet stars and luminous blue and red supergiants.

Key words: stars: early-type – stars: evolution – stars: fundamental parameters – stars: massive – galaxies: clusters: individual: R136 – Magellanic Clouds.

1 INTRODUCTION

The evolution of massive stars is still insufficiently understood, owing to uncertainties in nuclear reaction rates, stellar structure, internal mixing processes, and mass-loss properties (Langer 2012). The uncertainties increase with stellar mass (e.g. Martins & Palacios 2013). Binary and higher order multiple systems magnify the complexity and add additional evolutionary channels (e.g. Eldridge et al. 2017). The small number of massive and very massive stars (VMSs) raises the challenges to better understand the nature of such rare but important objects in vigorously star-forming galaxies. Metal-poor very massive stars (VMSs > 100 $M_\odot$; Vink et al. 2015) are believed to be progenitors of gamma-ray bursts and pair-instability supernovae and produce more metals than the entire stellar mass function below (e.g. Langer 2009; Kozyreva, Yoon & Langer 2014). In addition, with their strong outflows and high ionizing fluxes they dominate and shape the evolution of galaxies and are the main indicator of the star-forming rate in galaxies. Doran et al. (2013) confirmed the importance of VMS in the ionizing budget of young starburst regions

★ E-mail: j.m.bestenlehner@sheffield.ac.uk

© 2020 The Author(s)
Published by Oxford University Press on behalf of the Royal Astronomical Society

Downloaded from https://academic.oup.com/mnras/article/499/2/1918/5905414 by guest on 11 February 2026

like 30 Doradus providing evidence that those stars contribute vitally to the ionization and shaping of the interstellar environment in their host galaxies.

Based on ultraviolet (UV) and optical spectroscopy with the *Hubble Space Telescope* (*HST*), de Koter, Heap & Hubeny (1997, 1998) identified stars for the first time with initial masses exceeding 100 $M_\odot$ in the cluster R136 at the centre of NGC 2070 in the Large Magellanic Cloud (LMC). Based on spectral type calibrations and optical *HST* data, Massey & Hunter (1998) suggested that more than 10 VMS are located in R136. Crowther et al. (2010) identified stars with initial masses up to 320 $M_\odot$ within the cluster core albeit with large uncertainties in the mass estimate. The existence of such VMS challenges the canonical upper mass limit of 150 $M_\odot$ proposed by Figer (2005), and bring them into the predicted initial stellar mass range of pair-instability supernovae of 140–260 $M_\odot$ at low metallicity (Heger & Woosley 2002; Langer et al. 2007). The finding of stars with initial masses in excess of 150 $M_\odot$ is supported by Bestenlehner et al. (2011, 2014) and Hainich et al. (2014) based on spectroscopic analysis, and by Tehrani et al. (2019) through dynamical and spectroscopic analysis of Mk 34, the most massive binary star known today ($139^{+21}_{-18}\,M_\odot + 127^{+17}_{-17}\,M_\odot$). Those VMS might be formed in a similar way to low-mass stars (Krumholz 2015) or via stellar merger (Banerjee, Kroupa & Oh 2012). The latter formation channel may result in an apparent age younger than the lower mass cluster members (Schneider et al. 2014b).

The VLT-FLAMES Tarantula Survey (VFTS; Evans et al. 2011) is the largest spectroscopic survey of massive stars today. They obtained multi-epoch spectra of over 800 O, B, and Wolf–Rayet (WR) stars in the Tarantula Nebula covering NGC 2060 and NGC 2070 of the 30 Doradus region, but excluded the core of R136 due to crowding.

Sabín-Sanjulián et al. (2014, 2017) undertook a spectroscopic analysis of VFTS O dwarfs. Most O dwarfs in the Tarantula Nebula have weak winds and show a large dispersion in the wind–luminosity relation (WLR) for stars more luminous than $\log L/L_\odot > 5.1$. The mass discrepancy between evolutionary and spectroscopic masses is rather small, but evolutionary models systematically predict slightly large surface gravities (Sabín-Sanjulián et al. 2017). VFTS O giants and supergiants were spectroscopically analysed by Ramírez-Agudelo et al. (2017). The WLR agreed with the theoretical prediction by Vink, de Koter & Lamers (2000, 2001). Five stars are helium enriched and show only modest projected rotational velocities ($\upsilon \sin i$) that are not in agreement with the prediction of rotational mixing in main-sequence single-star stellar structure calculations (Brott et al. 2011; Köhler et al. 2015).

In addition, by studying VFTS luminous O, Of/WN, and WNh stars, Bestenlehner et al. (2014) found no correlation between projected rotational velocity and helium composition (Y) at the stellar surface, but they discovered a strong correlation of Y with mass-loss rate ($\dot{M}$) over stellar mass ($M_\star$) for $\log \dot{M}/M_\star > -6.5$. This suggests that rotational mixing is a relatively unimportant factor in helium enhancement for these stars with strong winds, but that shedding the stellar envelopes through mass-loss might be the key process in chemically enriching the stellar surface with nucleosynthesis products of these VMSs. Also for OB stars in the Small Magellanic Cloud (SMC), Ramachandran et al. (2019) did not find evidence for a correlation of chemical mixing with rapid rotation.

Based on pre-main-sequence stars and tracks, Cignoni et al. (2015) report that the star formation rate in the NGC 2070 complex peaked between 1 and 3 Myr ago. de Koter et al. (1997, 1998) and Massey & Hunter (1998) estimated an age around 2 Myr based on the brightest stars within and in close proximity to the dense central cluster R136. Crowther et al. (2016) inferred a median age of ∼1.6 Myr from UV calibration for the central stellar population of R136. Based on stars in the periphery of R136, Massey & Hunter (1998) found that the slope of the initial mass function (IMF) is consistent with a Salpeter IMF (Salpeter 1955). Correcting for the dynamical ejection of massive stars Banerjee & Kroupa (2012) suggested that the IMF of R136 has been most likely top-heavy.

Schneider et al. (2018b) combined the OB star results from VFTS and studied the massive star formation in 30 Doradus. They found that massive stars with all masses and ages are scattered throughout 30 Doradus. This suggests that they are not only formed in the dense stellar populations NGC 2070 or NGC 2060 but also in relative isolation in the field (Bressert et al. 2012). The formation of massive stars swiftly increased around 8 Myr ago by forming stars in the field which continued inside NGC 2060 (5.7 Myr ago) and NGC 2070 (3.6 Myr ago) with a declining star formation rate in the last 1 Myr. R136 formed last in the centre of NGC 2070. The IMF of 30 Doradus without R136 is densely populated up to 200 $M_\odot$, with a shallower power-law exponent of $1.90^{+0.37}_{-0.26}$ for stars more massive than 15 $M_\odot$ predicting more massive stars than inferred using the standard Salpeter (1955) 2.35 value (Schneider et al. 2018a).

The star cluster R136 in the centre of NGC 2070 had been excluded by the VFTS because of crowding. To add the missing mosaic and to enable studies of the entire massive star population up to 300 $M_\odot$ in 30 Doradus, Crowther et al. (2016, Paper I) observed the cluster R136 in the optical and UV with the instrument STIS aboard the *HST*. Paper I provides a far-UV spectroscopic census of R136 and studied the origin of He II λ1640 in young star clusters. This Paper II undertakes an optical spectroscopic analysis to aim for the physical properties of most massive stars in R136 using consistent optical diagnostics and spectroscopic tools to VFTS. The third paper (Caballero-Nieves et al., in preparation, Paper III) focuses on the blue optical observations deriving spectral types and investigating multiplicity and rotational properties of the stellar content of R136. A future study of this series will explore the UV properties of these stars with attention to the stellar wind parameters and investigate systematics between UV + optical and optical-only spectroscopic analyses (Brands et al., in preparation, Paper IV).

This paper is structured as follows. In Section 2, we summarize the spectroscopic and photometric data used in this work. Our spectroscopic and error analysis are described in Section 3. We present the results (Section 4) in the context of the Hertzsprung–Russell diagram (Section 4.1), their stellar masses and ages (Section 4.2), and their WLR (Section 4.3). In Section 5, we discuss the surface helium composition of our sample (Section 5.1) and place our results in the context of cluster age and IMF of R136 (Sections 5.2 and 5.3), ionizing and mechanical feedback of R136 (Section 5.4), and put R136 in the wider context as a stellar population within the Tarantula Nebula (Section 5.5). We conclude in Section 6.

2 OBSERVATIONAL DATA

2.1 Spectroscopic data

This study makes use of the blue-optical *HST*-STIS/G430M and H α *HST*-STIS/G750M observations described in Paper I. They cover a wavelength range from λ3793 to 4849 Å with a resolving power of ∼7700 at λ4400 Å (*HST*-STIS/G430M) and λ6482 to 7054 with a resolving power of ∼6000 at H α (*HST*-STIS/G750M), respectively.

For the spectroscopic analysis (Section 3), we require rectified and radial velocity corrected spectra. Based on the spectral classification for Paper III, we selected a synthetic template spectrum for each

Downloaded from https://academic.oup.com/mnras/article/499/2/1918/5905414 by guest on 11 February 2026

target, which is used as a reference spectrum to normalize and correct for radial velocity shifts. A single spectrum was created by stitching several grating settings together. Stars with $\log L/L_{\odot} < 5.3$ have low signal-to-noise (S/N) spectra and the uncertainties of the stellar parameters are systematically larger. Less luminous but cooler stars have stronger He I lines and we were still able to derive reasonable effective temperatures and luminosities.

We do not consider spectra with an S/N below 5 per resolution element and removed the blended object HSH95 118 (H118) from Hunter et al. (1995), which was heavily contaminated by bright nearby sources, and spectroscopic double line binaries (SB2, H42, and H77). Our sample of 55 stars consists of 22 apparent single stars, 7 potential spectroscopic binaries (SB1/SB2), 19 stars with low S/N, and 7 stars which show to some extend cross-contamination due to crowding. The spectral types are taken from Paper III. The spectral resolution of the G430M grating is higher than the typical value used for spectral classification. The spectral classification was performed on a degraded resolution but with an improved S/N. More details on spectral classification and observational properties of the sample will be discussed in Paper III.

2.2 Photometric data

We derived the stellar luminosity by modelling the stellar spectral energy distribution (SED) including the interstellar extinction (Section 3.5). The following photometric data were used: optical *HST*/WFC3 *F*438*W* (*B*-band) and *F*555*W* (*V*-band) from De Marchi et al. (2011) and near-infrared (near-IR) K_s-band photometry from Khorrami et al. (2017). For stars where the *HST*/WFC3 data were incomplete, the *HST*/WFPC2 *F*336*W* (*U* band) and *F*555*W* (*V* band) photometric data were used from Hunter et al. (1995). We applied the magnitudes offset to WFPC2 photometry, which were obtained by Crowther et al. (2016) to the *F*336*W* (Δmag $= -0.15$) and *F*555*W* (Δmag $= -0.17$) magnitudes.

Khorrami et al. (2017) adopted the instrumental zero-points and verified the VLT/SPHERE K_s-band photometry with the *K*-band fluxes/magnitudes of six stars from Crowther et al. (2010), which were inferred from flux calibrated VLT/SINFONI spectra or from VLT/MAD K_s photometry (Campbell et al. 2010). They were not able to verify the *J*-band photometry because the VLT/MAD observations used by Campbell et al. (2010) were taken in the *H* and K_s band. Therefore, we did not use the VLT/SPHERE *J*-band data in this study.

The derived *K*-band magnitudes on the basis of flux calibrated spectra are uncertain because they are not direct measurements of the *K*-band flux. Therefore, we cross-matched the Khorrami et al. (2017) K_s-band catalogue with the VLT/MAD K_s-band catalogue from Campbell et al. (2010). We recognized a slight disagreement between both coordinate systems with increasing distance from the frame centre of the VLT/SPHERE catalogue. We rotated the VLT/SPHERE coordinate system to match the VLT/MAD and both catalogues agree within 0.1 arcsec. In cases where we found multiple cross-matches, we selected the match with the smallest absolute *K*-band difference in the VLT/SPHERE and VLT/MAD photometry. Up to 16.7 mag, the standard deviation between the two photometric catalogues was nearly constant, but suddenly increased for fainter objects (Fig. 1). Therefore, we calculated the mean offset for stars brighter than 16.7 mag in both catalogues. In Fig. 1, we show the cross-correlation between the two photometric catalogues. The mean offset is 0.001 mag and is negligible compared to the photometric errors.

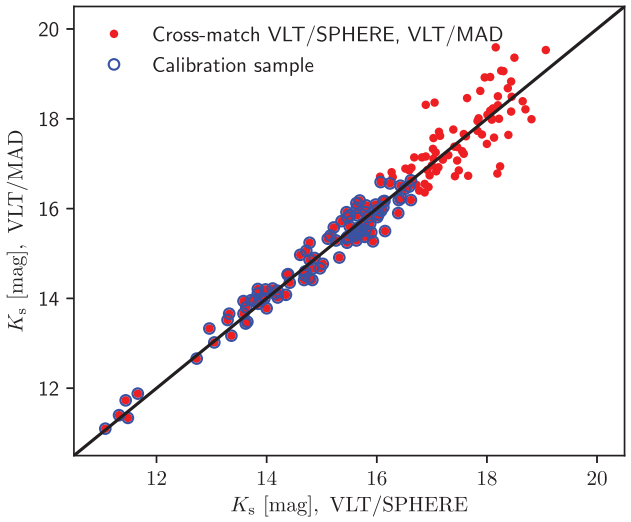


Figure 1. VLT/MAD (Campbell et al. 2010) versus VLT/SPHERE (Khorrami et al. 2017) K_s-band photometry. Stars brighter than 16.7 mag were used to determine the offset of 0.001 mag.

3 SPECTROSCOPIC ANALYSIS

In total, we analysed 55 stars and derived their stellar parameters. Paper I has observed R136 in the UV permitting measurements of terminal velocities (υ_{∞}) from P-Cygni resonance lines. Our sample of 55 stars comprises 50 targets that are in common with Paper I, as well as 5 additional targets (H120, H129, H139, H159, and H162) which lie beyond the MAMA detector and have no determined υ_{∞}. Terminal velocities of O stars can only be measured in the UV and are essential for calculating the mass-loss rates of our sample (Section 3.2). The UV wavelength range is crucial to constrain additional wind parameters such as velocity law exponent β and volume filling factor f_V of O stars (Paper IV).

We derive the line broadening parameters (Section 3.1) as a required input for the spectroscopic analysis, which is followed by a discussion on mass-loss rate scaling relations (Section 3.2). In Section 3.3, we describe our O star analysis, which employs the stellar atmosphere code FASTWIND (Santolaya-Rey, Puls & Herrero 1997; Puls et al. 2005; Rivero González et al. 2012a). We chose FASTWIND to analyse as many stars as possible to be comparable with the results from the VFTS (Evans et al. 2011) as most O stars were analysed with FASTWIND: O dwarfs (Sabín-Sanjulián et al. 2014, 2017), O giants and O supergiants (Ramírez-Agudelo et al. 2017), and their nitrogen abundances (Grin et al. 2017). The three WN5h stars in our sample are analysed with the stellar atmosphere code CMFGEN (Section 3.4; Hillier & Miller 1998). The bolometric luminosity is determined by matching photometric data with reddened theoretical SEDs (Section 3.5). In Section 3.6, we compare three transition objects, which are analysed with FASTWIND and CMFGEN, to estimate the systematics between both methods and codes.

FASTWIND and CMFGEN are non-local thermodynamic equilibrium (non-LTE) stellar atmosphere codes that consider spherical geometry, though take different approaches to the treatment of metal line blanketing. While CMFGEN considers all lines explicitly, FASTWIND uses an approximated approach. FASTWIND only calculates in detail the elements employed for the spectroscopic analysis and uses averages for background line opacity and emissivity. This approximation is most suitable for stars with optically thin winds and reproduces the line blanketing in a realistic way.

Downloaded from https://academic.oup.com/mnras/article/499/2/1918/5905414 by guest on 11 February 2026

3.1 Line broadening

To obtain the stellar spectral line broadening of the O-type stars, we use IACOB-BROAD (Simón-Díaz & Herrero 2014) to derive the projected rotational velocity ($\upsilon \sin i$) and macroturbulent velocity ($\upsilon_{\rm mac}$). IACOB-BROAD is an interactive analysis tool, that combines Fourier transformation and goodness-of-fit methods. The code is publicly available and is written in the interactive data language (IDL). A careful line broadening determination is, e.g. crucial to accurately derive surface gravities. An underestimation of the line broadening results in an over estimation of the surface gravity ($\log g$) and vice versa.

The S/N ratio of our spectra was too low for the faint metal lines to be used, which provide more accurate line broadening parameters. Instead our line broadening analysis relied on He I λ 4026 and 4471 and He II λ 4200 and 4542, but He I λ 4026 coincides with He II λ 4026 and could only be used for stars with $\lesssim 35\,000$ K. The quality of the spectra did not allow us to disentangle $\upsilon \sin i$ and $\upsilon_{\rm mac}$ broadening profiles. In addition, the He lines are also broadened by the Stark effect. He I lines disappear at temperatures around 45 000 K. He II lines could be used at temperatures above 40 000 K, but their line strength was only considerably above the noise level at temperatures $\gtrsim 50\,000$ K. The low S/N ratio made it difficult to find the first-order minimum when the Fourier transformation method of IACOB-BROAD was applied. Therefore, we used the goodness-of-fit assuming all broadening is produced by rotation and estimated a combined broadening $\upsilon \sin i_{\rm max}$ with $\upsilon_{\rm mac} = 0\,{\rm km\,s^{-1}}$ so that our values are an upper limit to the actual $\upsilon_{\rm rot}$. In our spectroscopic analysis, we also considered a broadening profile as if the line was only broadened by rotation. The adopted line broadening is listed in Table 1.

We could not use IACOB-BROAD for the three WNh stars because their emission lines are formed in the stellar wind above the hydrostatic layers. This does not only add an additional broadening due to the velocity gradient but also the measured $\upsilon \sin i$ is lower as a result of the differential rotation. To account for broadening caused by the wind velocity law, we convolved the synthetic spectrum with a rotation profile to match the line broadening of the observations (Figs S12–S14). We used N V at λ4604 and 4620 which have the closest line-forming regions to the hydrostatic layers for the given wavelength range. Like for the O stars, the macroturbulent velocity was set to zero assuming all broadening is produced by rotation. We estimated an upper $\upsilon \sin i$ limit of not more than $100\,{\rm km\,s^{-1}}$ for R136a2 and R136a3. The projected rotational velocity of R136a1 is somewhat higher and between 130 and $150\,{\rm km\,s^{-1}}$. Taking differential rotation into account, we adopted a $\upsilon \sin i_{\rm max} = 190\,{\rm km\,s^{-1}}$ for R136a1 and $150\,{\rm km\,s^{-1}}$ for R136a2 and R136a3 (Table 1).

3.2 Wind strength Q versus transformed mass-loss rate $\dot{M}_{\rm t}$

The strength of emission features scales not only with the mass-loss rate but also with the volume-filling factor ($f_{\rm v}$), terminal velocity, and radius of the star which are compressed into one parameter to reduce the effort when computing model grids. There are two ways to spectroscopically quantify mass-loss rates of hot massive stars using scaling relations. Stars with optically thin winds (OB stars), the wind strength parameter Q is usually applied (Puls et al. 1996; Sabín-Sanjulián et al. 2014, 2017; Holgado et al. 2018), where Q is proportional to the integrated optical depth over the resonance zone:

$$Q = \frac{\dot{M}\,[{\rm M_\odot yr^{-1}}]/\sqrt{f_{\rm v}}}{(R\,[R_\odot]\upsilon_\infty\,[{\rm km\,s^{-1}}])^{3/2}}, \tag{1}$$

and f_V has been set to unity (see Section 4.3). For optically thick conditions, there is an additional dependence on υ_∞ (e.g. Puls et al. 1996). The transformed radius (Schmutz, Hamann & Wessolowski 1989; Gräfener, Koesterke & Hamann 2002; Hamann & Gräfener 2004) or the equivalent approach of the transformed mass-loss rate ($\dot{M}_{\rm t}$, Bestenlehner et al. 2014) is usually used for optically thick winds (WR stars), where the line equivalent width is preserved:

$$\log(\dot{M}) = \log(\dot{M}_{\rm t}) + 0.5\log(f_{\rm v}) + \log\left(\frac{\upsilon_\infty}{1000\,{\rm km\,s^{-1}}}\right) + 0.75\log\left(\frac{L}{10^6 L_\odot}\right). \tag{2}$$

Both scaling relations are equivalent except for the exponent of the υ_∞ dependence, $\dot{M} \propto \upsilon_\infty^{3/2}$ (wind strength Q), and $\dot{M} \propto \upsilon_\infty$ (transformed mass-loss rate $\dot{M}_{\rm t}$). In our study, we compared both scaling relations and find that optically thin winds are preferably scaled with the wind strength parameter while optically thick winds are better scaled with the transformed mass-loss rate. If υ_∞ in the model has a reasonable value, the differences between both scaling relations are small. However, if the line is in emission and the terminal velocity of the synthetic spectrum is too high, the line centre is fitted well with the Q scaling relation, but the synthetic spectrum shows extended wings. This overestimates the actual mass-loss rate. By fitting Balmer lines in absorption, a degeneracy between $\log g$ and $\dot{M}$ can occur using the $\dot{M}_{\rm t}$ scaling relation. We used the $\dot{M}_{\rm t}$ scaling relation for R136a1, a2, a3, a5, b, and H36 and Q for the remaining O stars in our sample.

3.3 FASTWIND analysis

The majority of our targets (52 out 55) were analysed with the stellar atmosphere and radiative transfer code FASTWIND (Santolaya-Rey et al. 1997; Puls et al. 2005; Rivero González et al. 2012a) including nitrogen as an explicit element (Rivero González, Puls & Najarro 2011; Rivero González et al. 2012a, b). The three WN5h stars in the core of R136 (R136a1, a2, a3) have such strong stellar winds that they could not be analysed with FASTWIND.

The stellar parameters were determined using the automated spectroscopic analysis tool IACOB-Grid Based Automatic Tool (IACOB-GBAT; Simón-Díaz et al. 2011; Holgado et al. 2018). IACOB-GBAT uses a χ^2 algorithm to match the observed line profiles (here: H I, He I, and He II) with a grid of pre-computed FASTWIND synthetic spectra. Typically in normal χ^2 deep lines with many wavelength points dominate over narrow lines. To avoid these issues as much as possible, an optimized (iterative) strategy was incorporated in IACOB-GBAT which is described in appendix A of Holgado et al. (2018). Details and full description of the grid are given in Sabín-Sanjulián et al. (2014). At an effective temperature at optical depth $\tau = 2/3$ ($T_{\rm eff}$) of about $\gtrsim$45 000K, He I becomes weak or disappears and temperature determination using the He I–II ionization balance is not possible. Therefore, we recomputed the grid from Sabín-Sanjulián et al. (2014) for $T_{\rm eff}$ greater than 30 000 K and added nitrogen as an explicit element. The grid has a half-solar metallicity with respect to Asplund, Grevesse & Sauval (2005), except for CNO abundances. For those, we adopted values relative to hydrogen ($\epsilon_{\rm x} = \log(n_{\rm x}/n_{\rm H}) + 12$) according to Korn et al. (2002) ($\epsilon_{\rm C} = 8.06$, $\epsilon_{\rm N} = 7.01$, $\epsilon_{\rm O} = 8.37$). To match the observed nitrogen line intensity of the WNh stars, we used an N-abundance of $\epsilon_{\rm N} = 8.5$ (Section 3.4). Therefore, for CNO-processed atmospheres we set the nitrogen abundances to 8.5 (factor ∼30 enhancement) and an intermediate enrichment of 8.2

Downloaded from https://academic.oup.com/mnras/article/499/2/1918/5905414 by guest on 11 February 2026

Table 1. Stellar parameters.

ID	SpT	$\log L/L_\odot$	$T_{\rm eff}$ (K)	$\log g$ ($\rm cm\,s^{-2}$)	$\log \dot{M}/\sqrt{f_{\rm V}}$ ($\rm M_\odot\,yr^{-1}$)	Y	$\upsilon \sin i_{\rm max}$ ($\rm km\,s^{-1}$)	υ_∞ ($\rm km\,s^{-1}$)	$R_{\rm eff}$ ($R_\odot$)	Q_0 ($\rm ph\,s^{-1}$)	$M_{\rm V}$ (mag)	$M_{\rm K}$ (mag)	$A_{\rm K}$ (mag)	$M_{\rm sp}$ ($\rm M_\odot$)	$M_{\rm evo}$ ($\rm M_\odot$)	$M_{\rm evo,\,ini}$ ($\rm M_\odot$)	Age (Myr)	Comments (1)	Code
R136a1	WN5h^{CD98}	6.79 ± 0.10	$46\,000 \pm 2500$	–	-3.80 ± 0.20	0.50 ± 0.05	190	2600	39.2	50.59	−8.18	−7.68	0.26	–	215^{+45}_{-31}	251^{+48}_{-35}	$1.0^{+0.2}_{-0.2}$	s,N8.5	CMFGEN
R136a2	WN5h^{CD98}	6.75 ± 0.10	$50\,000 \pm 2500$	–	-3.84 ± 0.20	0.55 ± 0.05	150	2425	31.6	50.59	−7.80	−7.44	0.27	–	187^{+23}_{-33}	211^{+31}_{-32}	$1.2^{+0.2}_{-0.2}$	s,N8.5	CMFGEN
R136a3	WN5h^{CD98}	6.63 ± 0.10	$50\,000 \pm 2500$	–	-3.83 ± 0.20	0.55 ± 0.05	150	2400	27.5	50.47	−7.52	−7.31	0.26	–	154^{+28}_{-23}	181^{+29}_{-31}	$1.3^{+0.2}_{-0.2}$	s,N8.5	CMFGEN
R136a4	O3 V((f*))(n)	6.24 ± 0.18	$48\,000 \pm 5800$	4.1 ± 0.2	-5.69 ± 0.21	$0.26^{+0.16}_{-0.06}$	180	2475	19.1	50.06	−6.68	−5.66	0.26	167^{+98}_{-62}	86^{+27}_{-20}	89^{+28}_{-20}	$0.7^{+0.4}_{-0.6}$	c,N8.2	FASTWIND
R136a5	O2 I(n)f*	$6.29^{+0.10}_{-0.09}$	$47\,000 \pm 3300$	4.00 ± 0.15	$-4.52^{+0.19}_{-0.17}$	0.34 ± 0.10	100	3045	21.1	50.13	−6.83	−5.97	0.21	162^{+61}_{-45}	105^{+18}_{-15}	111^{+18}_{-15}	$1.0^{+0.3}_{-0.3}$	c,N8.5	FASTWIND
R136a5	O2 I(n)f*	$6.28^{+0.11}_{-0.10}$	$46\,000 \pm 2500$	4.00 ± 0.25	$-4.59^{+0.22}_{-0.20}$	0.30 ± 0.05	100	3045	21.6	50.07	−6.86	−5.97	0.21	171^{+133}_{-75}	96^{+19}_{-13}	104^{+18}_{-15}	$1.2^{+0.3}_{-0.3}$	c,N8.5	CMFGEN
R136a6	O2 I(n)f*p	6.27 ± 0.09	$53\,000 \pm 3500$	4.1 ± 0.3	-5.15 ± 0.17	$0.26^{+0.12}_{-0.06}$	160	2650	16.2	50.15	−6.46	−5.46	0.16	121^{+120}_{-60}	112^{+17}_{-15}	115^{+17}_{-15}	$0.4^{+0.3}_{-0.4}$	s,N8.2	FASTWIND
R136a7	O3 III(f*)^{MH98}	$6.25^{+0.18}_{-0.17}$	$49\,000 \pm 5500$	4.2 ± 0.5	$-5.45^{+0.24}_{-0.20}$	$0.30^{+0.25}_{-0.10}$	250	2710	18.5	50.07	−6.59	−5.65	0.21	199^{+430}_{-136}	88^{+29}_{-19}	93^{+28}_{-21}	$0.8^{+0.5}_{-0.7}$	c,N8.2	FASTWIND
R136b	O4 If	$6.35^{+0.15}_{-0.13}$	$37\,000 \pm 2400$	3.40 ± 0.25	$-4.61^{+0.23}_{-0.20}$	$0.30^{+0.11}_{-0.10}$	85	1400	36.2	50.15	−7.75	−7.04	0.21	120^{+99}_{-54}	93^{+26}_{-19}	104^{+31}_{-21}	$1.6^{+0.3}_{-0.3}$	s,N8.5	FASTWIND
R136b	O4 If	$6.34^{+0.12}_{-0.10}$	$35\,000 \pm 2500$	3.30 ± 0.25	$-4.55^{+0.22}_{-0.20}$	0.30 ± 0.05	85	1400	40.0	50.10	−7.70	−7.04	0.21	117^{+91}_{-51}	93^{+24}_{-13}	107^{+25}_{-17}	$1.7^{+0.2}_{-0.2}$	s,N8.5	CMFGEN
H30	O6.5 Vz	5.68 ± 0.14	$37\,000 \pm 3500$	3.90 ± 0.35	-6.06 ± 0.19	$0.24^{+0.09}_{-0.04}$	170	2490	16.9	49.22	−6.06	−5.07	0.23	83^{+103}_{-46}	40^{+7}_{-5}	41^{+8}_{-6}	$2.8^{+0.6}_{-0.6}$	s, bo	FASTWIND
H31	O2 V((f*))	6.01 ± 0.16	$48\,000 \pm 5000$	4.00 ± 0.25	-5.78 ± 0.20	$0.26^{+0.19}_{-0.06}$	130	2815	14.6	49.84	−6.11	−5.10	0.23	78^{+67}_{-36}	67^{+17}_{-13}	69^{+18}_{-13}	$1.1^{+0.5}_{-0.8}$	s,N8.2	FASTWIND
H35	O3 V	5.74 ± 0.18	$44\,000 \pm 5600$	4.0 ± 0.4	-5.88 ± 0.21	$0.24^{+0.10}_{-0.04}$	180	2770	12.7	49.51	−5.67	−4.68	0.19	59^{+82}_{-34}	47^{+11}_{-9}	48^{+11}_{-9}	$1.7^{+0.7}_{-1.1}$	s,N7.0	FASTWIND
H36	O2 If*	$6.33^{+0.12}_{-0.10}$	$52\,000 \pm 3400$	4.10 ± 0.35	$-4.74^{+0.19}_{-0.17}$	$0.20^{+0.07}_{-0.00}$	125	3500	18.0	50.21	−6.62	−5.74	0.21	148^{+176}_{-80}	118^{+24}_{-17}	122^{+23}_{-18}	$0.4^{+0.3}_{-0.4}$	s,N8.2	FASTWIND
H36	O2 If*	$6.29^{+0.13}_{-0.10}$	$48\,000 \pm 2500$	4.00 ± 0.25	$-4.78^{+0.22}_{-0.20}$	$0.25^{+0.00}_{-0.05}$	125	3500	20.2	50.12	−6.71	−5.74	0.21	149^{+116}_{-65}	103^{+21}_{-14}	109^{+22}_{-16}	$1.0^{+0.3}_{-0.3}$	s,N8.5	CMFGEN
H40	O3 V	5.88 ± 0.18	$45\,000 \pm 5600$	3.9 ± 0.4	-6.08 ± 0.21	$0.26^{+0.28}_{-0.06}$	150	2750	14.3	49.68	−5.98	−4.98	0.21	59^{+86}_{-35}	54^{+13}_{-12}	56^{+14}_{-12}	$1.6^{+0.7}_{-1.0}$	s,N7.0	FASTWIND
H45	O4: Vz	$5.84^{+0.17}_{-0.16}$	$42\,000 \pm 5000$	4.00 ± 0.45	$-6.58^{+0.24}_{-0.20}$	$0.24^{+0.31}_{-0.04}$	170	2620	15.7	49.55	−6.09	−5.07	0.21	90^{+152}_{-56}	50^{+12}_{-9}	52^{+12}_{-10}	$1.9^{+0.7}_{-1.0}$	SB?	FASTWIND
H46	O2-3 III(f*)	$6.16^{+0.18}_{-0.17}$	$49\,000 \pm 6000$	4.20 ± 0.35	$-5.16^{+0.24}_{-0.20}$	$0.24^{+0.13}_{-0.04}$	155	3440	16.6	49.99	−6.38	−5.41	0.21	160^{+198}_{-89}	80^{+24}_{-16}	83^{+24}_{-18}	$0.6^{+0.5}_{-0.6}$	c,N8.5	FASTWIND
H47	O2 V((f*))	$6.09^{+0.22}_{-0.21}$	$47\,000 \pm 7000$	4.0 ± 0.4	$-5.24^{+0.28}_{-0.22}$	$0.24^{+0.22}_{-0.04}$	165	3045	16.7	49.92	−6.37	−5.38	0.21	102^{+154}_{-61}	65^{+25}_{-15}	68^{+25}_{-17}	$1.1^{+0.6}_{-0.9}$	s,N8.2	FASTWIND
H48	O2-3 III(f*)	$6.05^{+0.21}_{-0.20}$	$49\,000 \pm 7200$	4.10 ± 0.35	$-5.33^{+0.27}_{-0.22}$	$0.24^{+0.22}_{-0.04}$	150	3045	14.6	49.88	−6.13	−5.12	0.21	98^{+122}_{-54}	66^{+22}_{-15}	68^{+23}_{-16}	$0.8^{+0.6}_{-0.8}$	s,N8.2	FASTWIND
H49	O3 V^{MH98}	5.89 ± 0.37	$48\,000 \pm 12\,000$	4.2 ± 1.0	-5.63 ± 0.32	$0.24^{+0.32}_{-0.04}$	155	2980	12.8	49.70	−5.80	−4.78	0.27	94^{+848}_{-85}	38^{+22}_{-13}	39^{+23}_{-14}	$1.0^{+1.3}_{-1.1}$	s/n	FASTWIND
H50	O3-4 V((f*))	5.71 ± 0.11	$42\,000 \pm 3000$	3.8 ± 0.4	-6.17 ± 0.18	$0.24^{+0.14}_{-0.04}$	200	2620	13.5	49.47	−5.79	−4.79	0.26	42^{+59}_{-25}	47^{+6}_{-6}	48^{+7}_{-6}	$2.2^{+0.5}_{-0.7}$	c,N7.0	FASTWIND
H52	O3-4 Vz	5.67 ± 0.16	$44\,000 \pm 4800$	4.00 ± 0.25	-5.92 ± 0.20	$0.24^{+0.08}_{-0.04}$	180	2820	11.8	49.44	−5.52	−4.52	0.23	51^{+42}_{-23}	45^{+9}_{-8}	46^{+9}_{-8}	$1.7^{+0.7}_{-1.1}$	s	FASTWIND
H55	O2 V((f*))z	5.76 ± 0.15	$47\,000 \pm 5000$	3.9 ± 0.3	-5.92 ± 0.19	$0.24^{+0.13}_{-0.04}$	130	2880	11.5	49.61	−5.59	−4.58	0.24	38^{+36}_{-19}	52^{+10}_{-9}	53^{+11}_{-9}	$1.5^{+0.6}_{-1.0}$	s,N7.0	FASTWIND
H58	O2-3 V:	5.94 ± 0.16	$50\,000 \pm 5900$	4.1 ± 0.4	-6.62 ± 0.20	$0.26^{+0.31}_{-0.06}$	150	2980	12.5	49.78	−5.84	−4.79	0.21	71^{+103}_{-42}	63^{+17}_{-12}	66^{+16}_{-13}	$0.8^{+0.6}_{-0.8}$	c, bo,N7.0	FASTWIND
H62	O2-3 V	5.75 ± 0.17	$49\,000 \pm 6200$	4.00 ± 0.45	-5.81 ± 0.20	$0.26^{+0.29}_{-0.06}$	170	2770	10.4	49.59	−5.41	−4.38	0.24	39^{+72}_{-25}	50^{+13}_{-10}	52^{+12}_{-10}	$1.1^{+0.7}_{-1.1}$	SB?,N8.2	FASTWIND
H64	O4-5 V:	$5.69^{+0.18}_{-0.17}$	$40\,000 \pm 5100$	3.9 ± 0.3	$-6.38^{+0.25}_{-0.21}$	$0.24^{+0.34}_{-0.04}$	180	1770	14.6	49.37	−5.86	−4.86	0.21	61^{+67}_{-32}	41^{+10}_{-7}	43^{+10}_{-8}	$2.3^{+0.8}_{-1.0}$	s	FASTWIND
H65	O4 V^{C16}	$5.74^{+0.17}_{-0.16}$	$42\,000 \pm 5200$	3.90 ± 0.55	$-6.17^{+0.24}_{-0.20}$	$0.24^{+0.35}_{-0.04}$	160	2540	14.1	49.48	−5.84	−4.85	0.21	57^{+141}_{-41}	45^{+11}_{-8}	47^{+11}_{-8}	$2.1^{+0.8}_{-1.1}$	s/n	FASTWIND
H66	O2 V-III(f*)	5.64 ± 0.21	$46\,000 \pm 6600$	4.10 ± 0.55	-5.65 ± 0.22	$0.24^{+0.21}_{-0.04}$	115	2590	10.4	49.44	−5.30	−4.31	0.24	50^{+135}_{-36}	42^{+12}_{-9}	42^{+12}_{-9}	$1.3^{+0.8}_{-1.3}$	s, bo,N8.2	FASTWIND
H68	O4-5 Vz	$5.73^{+0.23}_{-0.22}$	$43\,000 \pm 7000$	4.0 ± 0.4	$-6.89^{+0.29}_{-0.23}$	$0.24^{+0.28}_{-0.04}$	210	1910	13.3	49.47	−5.76	−4.74	0.21	64^{+101}_{-39}	42^{+13}_{-9}	44^{+14}_{-10}	$1.8^{+0.9}_{-1.3}$	s/n, bo	FASTWIND
H69	O4-5 Vz	5.51 ± 0.16	$41\,000 \pm 4600$	4.1 ± 0.3	-6.29 ± 0.20	$0.24^{+0.09}_{-0.04}$	130	2580	11.2	49.18	−5.32	−4.31	0.21	58^{+60}_{-30}	37^{+7}_{-6}	37^{+7}_{-6}	$2.1^{+0.8}_{-1.3}$	s	FASTWIND

Downloaded from https://academic.oup.com/mnras/article/499/2/1918/5905414 by guest on 11 February 2026

Table 1 – *continued*

ID	SpT	$\log L/L_\odot$	$T_{\rm eff}$ (K)	$\log g$ ($\rm cm\,s^{-2}$)	$\log \dot{M}/\sqrt{f_{\rm V}}$ ($\rm M_\odot\,yr^{-1}$)	Y	$\upsilon \sin i_{\rm max}$ ($\rm km\,s^{-1}$)	υ_∞ ($\rm km\,s^{-1}$)	$R_{\rm eff}$ ($R_\odot$)	Q_0 ($\rm ph\,s^{-1}$)	$M_{\rm V}$ (mag)	$M_{\rm K}$ (mag)	$A_{\rm K}$ (mag)	$M_{\rm sp}$ ($\rm M_\odot$)	$M_{\rm evo}$ ($\rm M_\odot$)	$M_{\rm evo,\,ini}$ ($\rm M_\odot$)	Age (Myr)	Comments (1)	Code
H70	O5 Vz	5.78 ± 0.18	$47\,000 \pm 6000$	4.20 ± 0.35	-5.96 ± 0.21	$0.24^{+0.16}_{-0.04}$	165	2670	11.7	49.57	−5.59	−4.56	0.27	80^{+94}_{-43}	51^{+13}_{-10}	52^{+13}_{-10}	$0.9^{+0.7}_{-0.9}$	SB?,N7.0	FASTWIND
H71	O2-3 V((f*))	5.56 ± 0.23	$48\,000 \pm 8000$	3.9 ± 0.7	-7.00 ± 0.24	$0.26^{+0.35}_{-0.06}$	140	2475	8.7	49.41	−5.03	−4.01	0.22	22^{+88}_{-17}	38^{+11}_{-9}	38^{+12}_{-9}	$1.2^{+1.1}_{-1.2}$	s,N7.0	FASTWIND
H73	O9.7-B0 V	5.27 ± 0.14	$33\,000 \pm 3600$	4.3 ± 0.4	–	$0.24^{+0.10}_{-0.04}$	125	–	13.2	48.31	−5.30	−4.32	0.21	127^{+184}_{-75}	26^{+4}_{-3}	27^{+4}_{-3}	$4.0^{+1.2}_{-1.4}$	s	FASTWIND
H75	O6 V	5.29 ± 0.22	$39\,000 \pm 6900$	4.3 ± 0.5	-6.41 ± 0.23	$0.24^{+0.28}_{-0.04}$	145	2550	9.7	48.84	−4.92	−3.90	0.19	68^{+142}_{-46}	28^{+7}_{-5}	28^{+7}_{-6}	$1.9^{+1.2}_{-1.9}$	SB?	FASTWIND
H78	O4: V	5.60 ± 0.24	$48\,000 \pm 8000$	4.20 ± 0.45	-6.00 ± 0.24	$0.24^{+0.33}_{-0.04}$	105	2375	9.1	49.41	−5.07	−4.05	0.24	48^{+87}_{-31}	39^{+13}_{-9}	40^{+13}_{-10}	$0.7^{+1.4}_{-0.7}$	SB?,N8.2	FASTWIND
H80	O8 V	5.15 ± 0.15	$35\,000 \pm 3800$	3.8 ± 0.4	-7.16 ± 0.20	$0.24^{+0.13}_{-0.04}$	155	1655	10.2	48.58	−4.91	−3.92	0.20	24^{+39}_{-15}	25^{+4}_{-3}	25^{+4}_{-3}	$4.2^{+1.4}_{-1.7}$	s	FASTWIND
H86	O5: V	5.26 ± 0.16	$41\,000 \pm 5000$	3.8 ± 0.4	-6.02 ± 0.20	$0.24^{+0.07}_{-0.04}$	175	2475	8.4	49.01	−4.69	−3.74	–	16^{+23}_{-9}	29^{+5}_{-5}	30^{+5}_{-5}	$2.7^{+1.2}_{-1.8}$	c	FASTWIND
H90	O4: V:	5.32 ± 0.13	$40\,000 \pm 3700$	4.1 ± 0.5	-6.15 ± 0.19	$0.24^{+0.19}_{-0.04}$	130	2475	9.5	48.96	−4.91	−3.91	0.25	41^{+83}_{-27}	31^{+5}_{-4}	32^{+5}_{-4}	$2.5^{+1.0}_{-1.6}$	s	FASTWIND
H92	O6 Vz	5.26 ± 0.14	$39\,000 \pm 4000$	4.00 ± 0.45	-7.06 ± 0.19	$0.24^{+0.23}_{-0.04}$	150	2080	9.4	48.87	−4.87	−3.86	0.24	32^{+56}_{-21}	30^{+4}_{-4}	30^{+5}_{-4}	$2.8^{+1.1}_{-1.7}$	s	FASTWIND
H94	O4-5 Vz	5.52 ± 0.23	$48\,000 \pm 8200$	4.20 ± 0.45	-6.50 ± 0.24	$0.24^{+0.33}_{-0.04}$	170	2490	8.3	49.32	−4.90	−3.85	0.21	40^{+71}_{-26}	37^{+11}_{-9}	37^{+11}_{-8}	$0.6^{+1.6}_{-0.6}$	s,N7.0	FASTWIND
H108	O Vn	5.04 ± 0.24	$43\,000 \pm 7600$	4.20 ± 0.55	-7.31 ± 0.26	$0.24^{+0.31}_{-0.04}$	260	1040	6.0	48.75	−4.00	−2.98	–	21^{+49}_{-14}	23^{+6}_{-5}	23^{+6}_{-5}	$0.0^{+3.5}_{-0.0}$	s/n	FASTWIND
H112	O7-9 Vz	5.21 ± 0.19	$36\,000 \pm 6000$	4.3 ± 0.7	–	$0.26^{+0.35}_{-0.06}$	160	–	10.3	48.57	−4.93	−3.92	0.21	77^{+311}_{-62}	25^{+6}_{-4}	26^{+6}_{-5}	$3.3^{+1.5}_{-2.4}$	s/n, bo	FASTWIND
H114	O5-6 V	5.25 ± 0.21	$44\,000 \pm 6800$	4.2 ± 0.5	-7.33 ± 0.23	$0.26^{+0.35}_{-0.06}$	100	1770	7.3	48.98	−4.48	−3.44	0.21	31^{+67}_{-21}	29^{+7}_{-6}	29^{+7}_{-6}	$0.8^{+2.0}_{-0.8}$	s/n	FASTWIND
H116	O7 V	4.84 ± 0.16	$34\,000 \pm 4100$	3.70 ± 0.55	-7.71 ± 0.24	$0.26^{+0.35}_{-0.06}$	185	960	7.6	48.22	−4.21	−3.23	0.19	10^{+26}_{-7}	19^{+3}_{-2}	19^{+3}_{-3}	$5.0^{+2.1}_{-3.0}$	s/n	FASTWIND
H120	–	4.81 ± 0.22	$37\,000 \pm 6800$	4.3 ± 0.6	–	$0.24^{+0.22}_{-0.04}$	150	–	6.2	48.25	−3.87	−2.86	0.12	28^{+81}_{-21}	19^{+4}_{-4}	19^{+4}_{-3}	$1.1^{+3.7}_{-1.1}$	s/n	FASTWIND
H121	O9.5 V	4.86 ± 0.16	$34\,000 \pm 4800$	4.20 ± 0.65	–	$0.30^{+0.35}_{-0.10}$	150	–	7.8	48.05	−4.22	−3.22	0.20	35^{+118}_{-27}	20^{+3}_{-3}	20^{+3}_{-3}	$4.1^{+1.9}_{-3.1}$	s/n, bo	FASTWIND
H123	O6 V	5.01 ± 0.22	$41\,000 \pm 6500$	4.10 ± 0.45	-7.48 ± 0.24	$0.26^{+0.35}_{-0.06}$	120	1615	6.3	48.67	−4.09	−3.07	0.19	18^{+31}_{-12}	23^{+5}_{-4}	23^{+5}_{-4}	$1.5^{+2.1}_{-1.6}$	s/n	FASTWIND
H129	–	4.37 ± 0.26	$37\,000 \pm 8200$	4.00 ± 0.65	–	$0.24^{+0.35}_{-0.04}$	135	–	3.7	47.91	−2.76	−1.80	–	5^{+18}_{-4}	13^{+3}_{-3}	13^{+3}_{-3}	$0.1^{+8.6}_{-0.1}$	s/n	FASTWIND
H132	O7: V	5.05 ± 0.20	$39\,000 \pm 5800$	4.0 ± 0.5	–	$0.26^{+0.35}_{-0.06}$	115	–	7.4	48.68	−4.32	−3.34	0.21	20^{+44}_{-14}	23^{+5}_{-4}	24^{+5}_{-4}	$2.6^{+1.5}_{-2.4}$	s/n	FASTWIND
H134	O7 Vz	4.81 ± 0.17	$36\,000 \pm 4800$	4.00 ± 0.35	-7.67 ± 0.23	$0.24^{+0.30}_{-0.04}$	105	1170	6.6	48.25	−3.96	−2.96	0.18	16^{+20}_{-9}	19^{+3}_{-3}	20^{+3}_{-3}	$3.5^{+1.9}_{-2.8}$	s/n	FASTWIND
H135	B	4.89 ± 0.17	$33\,000 \pm 4900$	4.0 ± 0.5	–	$0.26^{+0.35}_{-0.06}$	125	–	8.6	48.05	−4.37	−3.40	0.23	27^{+54}_{-18}	19^{+3}_{-3}	20^{+3}_{-3}	$4.8^{+2.1}_{-3.0}$	s/n	FASTWIND
H139	–	4.90 ± 0.17	$38\,000 \pm 5100$	4.00 ± 0.45	–	$0.26^{+0.35}_{-0.06}$	85	–	6.5	48.48	−4.01	−3.04	0.19	15^{+29}_{-10}	21^{+4}_{-3}	21^{+4}_{-3}	$2.6^{+1.7}_{-2.5}$	s/n, bo	FASTWIND
H141	O5-6 V^{C16}	4.79 ± 0.21	$32\,000 \pm 6000$	3.6 ± 0.7	–	$0.24^{+0.28}_{-0.04}$	120	–	8.1	48.07	−4.24	−3.29	0.20	10^{+38}_{-8}	17^{+4}_{-3}	17^{+4}_{-3}	$5.9^{+2.9}_{-3.9}$	s/n	FASTWIND
H143	O8-9 V-III	5.18 ± 0.20	$39\,000 \pm 6000$	4.2 ± 0.5	-6.35 ± 0.23	$0.24^{+0.35}_{-0.04}$	150	1480	8.5	48.78	−4.62	−3.65	0.27	42^{+90}_{-28}	26^{+6}_{-4}	26^{+6}_{-4}	$2.2^{+1.3}_{-2.1}$	s/n	FASTWIND
H159	–	4.93 ± 0.28	$36\,000 \pm 8900$	4.3 ± 0.9	–	$0.24^{+0.35}_{-0.04}$	150	–	7.5	48.30	−4.24	−3.23	0.25	41^{+277}_{-36}	18^{+6}_{-4}	19^{+6}_{-4}	$2.6^{+2.9}_{-2.6}$	s/n, bo	FASTWIND
H162	–	4.87 ± 0.39	$37\,000 \pm 13\,000$	4.3 ± 1.0	–	$0.24^{+0.35}_{-0.04}$	150	–	6.6	48.36	−3.98	−3.03	0.20	32^{+284}_{-28}	15^{+6}_{-4}	15^{+6}_{-4}	$1.7^{+5.6}_{-1.7}$	s/n	FASTWIND
H173	O9 + V^{C16}	4.65 ± 0.33	$30\,000 \pm 10\,000$	4.30 ± 0.85	–	$0.24^{+0.25}_{-0.04}$	140	–	7.8	47.14	−3.97	−3.03	0.17	45^{+271}_{-38}	13^{+4}_{-3}	13^{+4}_{-3}	$4.0^{+5.2}_{-4.0}$	s/n	FASTWIND

Notes. Spectral types are from Paper III, (*CD*98) and (*MH*98) are optical spectral types from Crowther & Dessart (1998) and Massey & Hunter (1998), respectively. (*C*16) are spectral types from Paper I based on UV spectra. (1) apparent single star (s), potential spectroscopic binary (SB?), low S/N (s/n), cross-contamination as a result of crowding (c), only blue-optical wavelength range was used for the spectroscopic analysis (bo), nitrogen abundances: N7.0 $\equiv \epsilon_{\rm N} = 7.01$, N8.2 $\equiv \epsilon_{\rm N} = 8.2$, and N8.5 $\equiv \epsilon_{\rm N} = 8.5$. Uncertainties are 1σ confidence ranges.

Downloaded from https://academic.oup.com/mnras/article/499/2/1918/5905414 by guest on 11 February 2026

(factor ∼15 enhancement), with carbon and oxygen been reduced accordingly.

Based on photo-ionization nebular models, Pellegrini, Baldwin & Ferland (2011) derived an N-abundance of $\epsilon_{\rm N} = 7.09$ for 30 Dor, with C-abundance not measured. The evolutionary models used in this study (Brott et al. 2011; Köhler et al. 2015) adopted a nitrogen base line of $\epsilon_{\rm N} = 6.90$, which represents the LMC average (Hunter et al. 2007; Brott et al. 2011). The value of Korn et al. (2002) lies somewhat in between and has been therefore chosen. However, the actual N-abundance of our objects is not determined in this study, but we provide an indication, if N is enriched at the surface for stars hotter than ∼ 45 000 K. The assumed N-abundance can affect the temperature determination for those stars, where $T_{\rm eff}$ is based on the ionization balance of N IV and N V. The degeneracy between $T_{\rm eff}$ and N-abundances is discussed in Section 3.6.

The stellar parameters were derived using the following spectral lines: Balmer Hα and Hγ–ϵ, He I λ4026, 4121, 4144, 4388, 4471, and 4713, He II λ4026, 4200, 4542, 4686, N III λ4634 and 4641, N IV λ4058 and 6381, and N V λ4604 and 4620 (Fig. S4). We applied IACOB-GBAT to all O-type stars in our sample and all stellar parameters were set free ($T_{\rm eff}$, $\log g$, Q, velocity law exponent β, helium mass fraction Y, and microturbulent velocity $\upsilon_{\rm mic}$). The microturbulent velocity was treated depth independent and homogeneous winds were assumed with $f_{\rm v} = 1.0$. IACOB-GBAT aims at a global optimization, uses all lines in parallel to derive all parameters in parallel, and takes into account correlations between the various parameters. The largest weight on $T_{\rm eff}$ is from the ionization balance of the He I and II while $\log g$ is mainly constrained by Hγ, δ, ϵ and Q by Hα and He II λ4686 assuming a typical velocity law exponent β for a given luminosity class (Section 3.3.1). Using Q, mass-loss rates are calculated with the wind strength scaling relation (Section 3.2) and terminal velocities from Paper I, if available (Table 1). Stellar radii ($R_{\rm eff}$) were calculated with $L = 4\pi\sigma R^2 T_{\rm eff}^4$ and Stefan–Boltzmann constant σ to scale $\dot{M}$ with Q. He-abundances are determined by the line ratio of hydrogen and helium lines, while $\upsilon_{\rm mic}$ is constrained by the line strength of He lines. This results in a degeneracy between Y and $\upsilon_{\rm mic}$ (Section 3.3.2).

For stars hotter than $\gtrsim$40 000 K, we adjusted the temperature by eye using the ionization balance of the nitrogen lines and adjusting the value of $\log g$. We ran IACOB-GBAT with a fixed temperature (Fig. S2). If $\log g$ was different to the assumed value, we checked the nitrogen ionization balance again and reran IACOB-GBAT. We iterated until the temperature and surface gravity converged.

IACOB-GBAT provides the uncertainties associated with each parameter and takes into account correlations between the various parameters. In some cases, the S/N ratio of the spectrum was so low, that all stellar parameters appeared to be degenerate (Fig. S1). Even though the χ^2 distribution was not completely flat, we were unable to derive an error. In such cases, we set free only two parameters at a time $T_{\rm eff}$ and $\log g$, Q and β and, Y and $\upsilon_{\rm mic}$ while the others were fixed. In this way, the χ^2 distribution was better characterized and errors could be to some extent estimated. Such stars are labelled as low S/N objects. The lower bound of Y was considerably below the physical limit ∼ 0.25 for some stars. In these cases, we truncated the lower error such that the lower limit was not below 0.2.

The results with their uncertainties (1σ) are given in Table 1.

3.3.1 *Degeneracy of β-type velocity law and mass-loss rate*

The velocity field in the stellar atmosphere codes is parametrized by a β-type velocity law. Smaller values of β correspond to larger velocity gradients ($\mathrm{d}\upsilon/\mathrm{d}r$) in the inner and lower $\mathrm{d}\upsilon/\mathrm{d}r$ in the outer wind and vice versa. For example, larger values of β lead to a denser wind in the onset region of the flow and result in a lower mass-loss rate estimate. The β-type velocity law and mass-loss rate are degenerate in the absence of necessary diagnostics and/or too weak stellar winds. The stellar spectrum can be matched with several sets of β and $\dot{M}$. Based on theoretical predictions, typical β exponents are between 0.8 and 1.0 for dwarfs and giants and between 0.9 and 1.1 for supergiants (Muijres et al. 2012). Based on a study of more than 250 O stars, Holgado et al. (2018) noted that for supergiants best-fitting models have preferences towards $\beta = 1.2$, even though only a lower limit could be determined. Therefore, we only allowed values of β to be 0.8, 1.0, and 1.2 for dwarfs and giants and 1.0, 1.2, and 1.5 for supergiants. A more detailed discussion on the effect of varying β in the determination of $\dot{M}$ can be found in Markova et al. (2005) and Holgado et al. (2018).

3.3.2 *Degeneracy of microturbulent velocity and He-abundances*

The microturbulent velocity ($\upsilon_{\rm mic}$) does not only broaden the spectral lines but also modifies the line strength of e.g. He I–II and N III–IV–V depending on their equivalent widths. As a consequence, not only the derived chemical abundances can be affected when an inaccurate $\upsilon_{\rm mic}$ is selected but also the effective temperature, if the line is used as a temperature diagnostic. The microturbulent velocity can be accurately constrained if the spectra are of high S/N and the number of available spectral lines of the same ion is large enough to achieve a consistent spectroscopic fit to all spectral lines. However, in cases where the spectrum has a low S/N ratio the degeneracy is more difficult to resolve. A large microturbulent velocity is favoured because of the low S/N, which leads to an underestimation of the derived He-abundance. Therefore, we only allowed typical O stars $\upsilon_{\rm mic}$ of 5 and 10 km s^{-1}, even though higher velocities are possible as well, in particular for supergiants.

3.4 CMFGEN analysis

The three core WNh stars R136a1, a2, and a3 plus three supergiants that were also modelled with FASTWIND, R136b, R136a5 and H36, were analysed with the stellar atmosphere and radiative transfer code CMFGEN (Hillier & Miller 1998) using the method described in Bestenlehner et al. (2014). Initial estimates of the stellar parameters were derived with the grid from Bestenlehner et al. (2014) with either half solar $\epsilon_{\rm N} = 7.44$ or enriched 8.5 nitrogen abundances. We computed extra grids of stellar atmospheres around the preferred stellar parameter space of the initial estimates with an extended atomic model and varying $T_{\rm eff}$, $\dot{M}$, β-type velocity law, and helium abundances. Effective temperatures of WR stars are usually defined at $\tau = 10$ or 20 ($T_\star$). In the case of the three WNh stars, the differences between $T_{\rm eff}$ and $T_\star$ are rather small ($\lesssim$ 1 per cent) and largely depend on the velocity law (Section 4.3). The gravity was fixed for R136a1, a2, and a3 to 4.0 as $\log g$ cannot be derived from emission lines of the optically thick WNh star winds, but varied for R136a5, R136b, and H36. Based on the electron scattering wings, the wind volume filling factor ($f_{\rm v}$) was set to 0.1 and the terminal velocities were taken from Paper I. The grid of stellar atmospheres contains the following element ions: H I, He I–II, C III–IV, N III–V, O III–VI, Ne III–VI, Si IV, P IV–V, S IV–VI, Fe IV–VII, and Ni IV–VI. $\upsilon_{\rm mic}$ was set to 10 km s^{-1}.

We used the same line diagnostics as described in Section 3.3 for the spectroscopic analysis with FASTWIND (Fig. S4). Stellar parameters are given in Table 1.

Downloaded from https://academic.oup.com/mnras/article/499/2/1918/5905414 by guest on 11 February 2026

3.5 Luminosity and reddening

To derive the bolometric luminosity ($L_{\rm bol}$) and estimate the interstellar extinction towards our targets, we match the model SED in the optical with B ($F438W$), V ($F555W$) from De Marchi et al. (2011) or B ($F438W$), V ($F555W$) from Hunter et al. (1995) and near-IR K_s from Khorrami et al. (2017) (top panel of Fig. S4). We extracted intrinsic U, B, V, and K_s colours from the modelled SED by applying approximated filter functions for each filter and calculated the extinctions $E(B-V)$ and $E(V-K_s)$.

In principle, one should use R_{5495} and $E(4405-5495)$ to define the amount and type of extinction, respectively, instead of R_V and $E(B-V)$ which, in general, depend on both and on the input SED. However, for the case where we are analysing hot stars with low extinction, as it is the case here, there is little difference between R_{5495} and R_V or between $E(4405-5495)$ and $E(B-V)$ (Fig. 3 of Maíz Apellániz 2013). The reddening parameter R_V is derived using the following relation inferred from the reddening law by Maíz Apellániz et al. (2014):

$$R_V = 1.12 \times E(V-K_{\rm s})/E(B-V) - 0.18. \quad (3)$$

In cases where only U and V optical magnitudes are available (Hunter et al. 1995), we obtained $E(B-V)$ and R_V by fitting the U, V, and K_s bands with the model SED and reddening law by Maíz Apellániz et al. (2014). The derived luminosities are anchored on the K_s-band flux as the extinction near-IR A_{K_s} is much smaller than optical A_V. In this way, we are able to determine reliable $L_{\rm bol}$ adopting a distance modulus of 18.48 mag (Pietrzyński et al. 2019).

In some cases, we inferred an unusually high $R_V > 5.0$ as a result of crowding. The B and V from De Marchi et al. (2011) showed an inconsistency between crowded regions and stars in relative isolation. R_V defines the overall shape of the reddening law and connects the optical with the near-IR. By using the K_s-band flux to derive the luminosity, the influence of R_V is rather small. There were also a few targets with an unusually low $R_V < 2.5$, which is an indication of a near-IR excess. To tackle the issue, we applied sigma clipping to our R_V values and derived an average $R_V = 4.18 \pm 0.38$ and $A_{K_s} = 0.21 \pm 0.03$. The values are similar to what Doran et al. (2013) had obtained within the R136 region ($R_V = 4.2$ and $A_{K_s} = 0.17$). In cases where $R_V > 5.0$, we set $A_{K_s} = 0.21$ to avoid overestimating the luminosity of the star. We still propagated the potential larger A_{K_s} value into the upper luminosity error. If $R_V < 2.3$ (2σ below the standard $R_V = 3.1 - 2 \times 0.4$) we anchored the luminosity on the V band and estimated A_V on the basis of $E(B-V)$ and the average $R_V = 4.18 \pm 0.38$ (H86, H108, H129). No A_K is listed in Table 1 for those stars.

Luminosities, absolute magnitudes, and extinction for each star are listed in Table 1.

3.6 Systematics between FASTWIND and CMFGEN analysis methods

For our analysis, we used two different approaches. The three WN5h stars (Section 3.4) were analysed with the method described in Bestenlehner et al. (2014) using a grid of synthetic spectra computed with CMFGEN (Hillier & Miller 1998) and N-abundances of $\epsilon_{\rm N} = 7.44$ and 8.5. The O stars were analysed with IACOB-GBAT (Simón-Díaz et al. 2011) based on a grid of synthetic spectra computed with FASTWIND (Santolaya-Rey et al. 1997; Puls et al. 2005; Rivero González et al. 2012a) and N-abundances of $\epsilon_{\rm N} = 7.01$, 8.2, and 8.5. The grid, to explore the O star parameter space, can be computed faster with FASTWIND than with CMFGEN, but FASTWIND was not designed to analyse stars with strong and optically thick winds such as the three WN5h stars in the core of R136.

Massey et al. (2013) compared both stellar atmosphere codes for the physical properties of SMC and LMC O type stars. The systematic difference is small compared to our error margins. However, systematic differences between the codes might be larger at the transition from optically thin to optically thick winds at the edge of the FASTWIND comfort zone. Two diverse analysis methods were used as well which could add to the systematics (Sections 3.3 and 3.4).

We compared the results for three objects, H36, R136a5, and R136b, at the transition from optically thin to optically thick winds to identify potential systematics between these two analysis approaches. Stellar parameters are given in Table 1 and spectral fits are shown in Figs S5–S7. The results for R136a5 are comparable between the methods. The inferred temperature and surface gravity for R136b are lower for the CMFGEN analysis method. Holgado et al. (2018) found a similar systematic towards lower $\log g$ and $T_{\rm eff}$ for CMFGEN, which results from deeper predicted line profiles of He II λ4200/4542.

A large temperature difference occurs for H36. The FASTWIND analysis method results in an effective temperature of 52 000K while the CMFGEN one leads to 48 000K. Model comparison showed that CMFGEN and FASTWIND are very consistent around 50 000 K. A test calculation with $T_{\rm eff} = 52\,000$K using CMFGEN showed, that the N V at λ4604 and 4620 and N IV at λ4058 can be simultaneously fitted with the lower nitrogen abundance of $\epsilon_{\rm N} = 8.2$ from the FASTWIND model. Thus, the different results on $T_{\rm eff}$ are presumable a consequence of the different assumptions on the nitrogen abundance. With the lack of wavelength coverage beyond λ4850 to observe N V at λ4945, we are not able to rule out one of the two possible temperatures or nitrogen abundances. To fit Hα and He II λ4686 at the same time, an unphysically low helium abundance is required, $Y \sim 20$ per cent in mass fraction (Fig. S7). This may point to an excess in the Hα emission. Though we are not sure about the nature of such an excess, it might be due to differential effects of clumping in the Hα and He II λ4686 line-forming region or could be an indication of binarity. Save for H36, the stellar parameters barely affect the results on the stellar mass and age. The lower temperature based on the CMFGEN fit of H36 would lead to an older age and lower stellar mass (Table 1).

4 RESULTS

4.1 Hertzsprung–Russell diagram of R136

In Fig. 2, we show the Hertzspung–Russell diagram (HRD) for R136. Stars appearing to be single are plotted as red dots (22 stars), probable spectroscopic binaries are blue stars (7 stars), targets with low S/N spectra are black pluses (19 stars) while contaminated spectra by nearby stars as a result of crowding are shown as green diamonds (7 stars). SB2s (H42 and H77) and heavily contaminated/blended (H118) stars are not included in Fig. 2 and were excluded from the analysis as sensible stellar parameters could not be derived. Stars below our nominal S/N limit ($\lesssim$7) roughly follow a diagonal line, which is indicated by a black dotted line in Fig. 2. The zero-age main-sequence (ZAMS), 0.8, 1.6, and 2.5 Myr isochrones with $\upsilon_{\rm rot} = 180\,{\rm km\,s^{-1}}$ are visualized in Fig. 2 as well (Brott et al. 2011; Köhler et al. 2015, hereafter BONN). The 1.6 Myr isochrones correspond to the median age of R136 (Section 5.2). Based on their position in the HRD, stars with luminosities $\log L/L_\odot \gtrapprox 5.5$ are all younger than 2.5 Myr. Below this threshold, there are stars that are potentially older than 2.5 Myr. However, the isochrones are closer to each other

Downloaded from https://academic.oup.com/mnras/article/499/2/1918/5905414 by guest on 11 February 2026

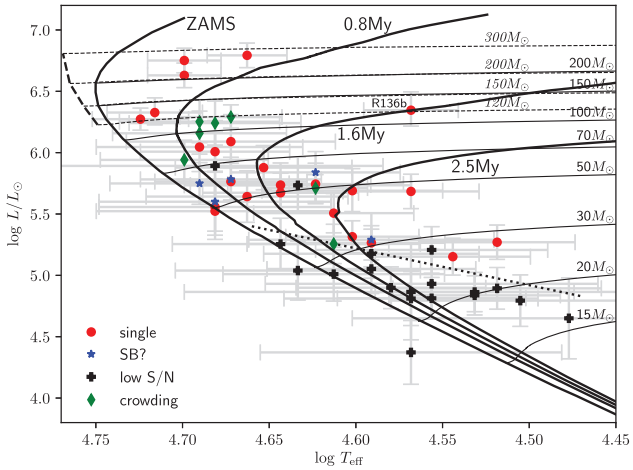


Figure 2. HRD of our analysed stars indicating single stars (red dots), probable spectroscopic binaries (blue stars), stars with low S/N spectra (black pluses), and contaminated objects by nearby stars (green diamonds). Evolutionary tracks are from Brott et al. (2011) and Köhler et al. (2015) (solid black lines) and Yusof et al. (2013) (dashed black lines). ZAMS and 0.8, 1.6, 2.5 Myr isochrones are shown as well with an initial rotation rate of 180 km s^{-1}. Black dotted line indicates our nominal S/N limit.

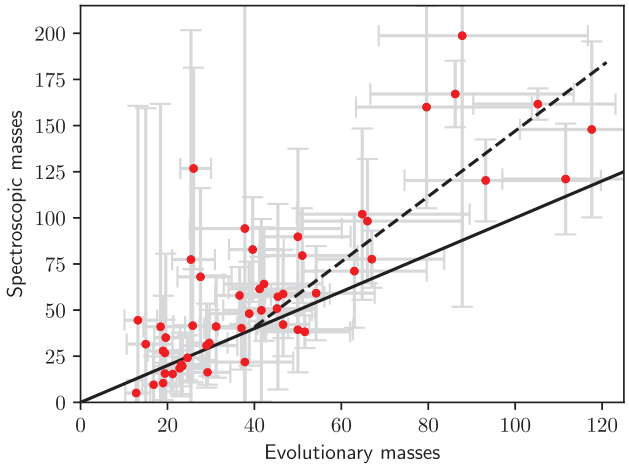


Figure 3. Spectroscopic versus current evolutionary masses: even though both masses mostly agree within their uncertainties, a systematic offset develops towards higher masses (dashed line).

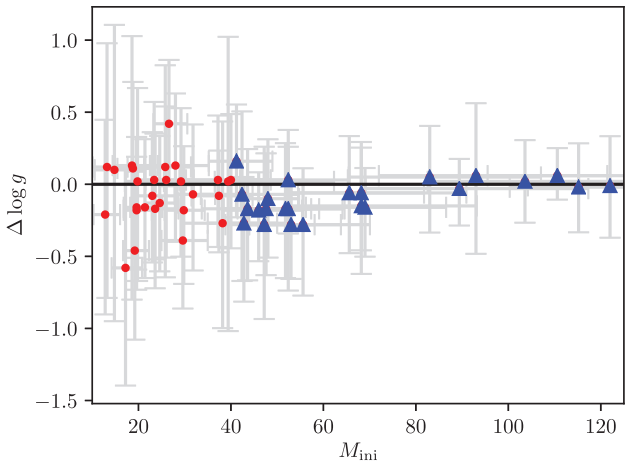


Figure 4. Spectroscopic minus evolutionary gravities against initial stellar mass (red dots). Stars with initial mass >40 M$_\odot$ are shown as blue triangles. Up to $\sim$ 80 M$_\odot$ spectroscopic gravities are systematically smaller than evolutionary gravities, which is expected for the negative mass discrepancy.

and the position of these stars overlap with both isochrones within their uncertainties. An age determination based on the location in the HRD is inaccurate as the uncertainties of the stellar parameters of those stars are large. We applied the more sophisticated tool such as BONNSAI[1] (Schneider et al. 2014a) to quantify the age distribution in R136, which is described in Section 4.2.

At the high-mass end, we also added the 120, 150, 200, and 300 M$_\odot$ tracks from Yusof et al. (2013, hereafter GENEVA). BONN and GENEVA tracks are comparable, but there is an offset for the location of the ZAMS. The difference between tracks is that the stellar structure models by the BONN group allow stellar envelope inflation to occur as a result of their proximity to the Eddington limit (Sanyal et al. 2015). Therefore, these tracks have cooler effective temperatures already at the high-mass ZAMS (log $L/L_\odot \gtrsim 6.5$). The mass range of our targets are between 10 and 300 M$_\odot$ based on the evolutionary tracks. Most stars populate the region near the ZAMS. R136b appears to be isolated from the rest of our sample. This star has the lowest determined surface gravity of our entire sample. To match the strong nitrogen lines in the spectrum of R136b, a high N-abundance similar to the WNh stars was required, which indicates that carbon and oxygen are largely converted into nitrogen as a result of the CNO cycle (Fig. S6).

4.2 Stellar masses and ages

Stellar evolutionary masses and ages for our targets are derived with the BONN Stellar Astrophysics Interface (BONNSAI; Schneider et al. 2014a). BONNSAI is a Bayesian tool to calculate the probability distributions of fundamental stellar parameters for a given set of observed stellar parameters including their uncertainties. It also provides predictions of unobserved quantities and tests stellar evolutionary models. Our input to BONNSAI were luminosity, effective temperature, surface gravity, and helium abundances. WNh stars analysed with CMFGEN had too strong stellar winds to constrain log g.

[1] https://www.astro.uni-bonn.de/stars/bonnsai/

For those objects, the surface gravity was not an input parameter to BONNSAI.

In Fig. 3, we compare the spectroscopic masses with the evolutionary masses ($M_{\rm evo}$) derived with BONNSAI. The three WNh stars have no log g determination and are excluded from Figs 3 to 5. For the evolutionary masses, we used the mode of the probability distribution function (PDF). Spectroscopic masses were calculated with the surface gravities and radii given in Table 1. With increasing stellar mass, we see a systematic trend towards larger spectroscopic than evolutionary masses (positive mass discrepancy), especially for $M_{\rm evo} \gtrsim 70$ M$_\odot$.

To investigate this further, we compare the differences of spectroscopic log g versus the mode of the BONNSAI probability distribution of log g. From Fig. 4 it seems that up to 80 M$_\odot$ the stellar models prefer higher log g values which would also place the stars closer to the ZAMS. For those objects, spectroscopic gravities are lower than evolutionary values, which is the typical case for the negative mass discrepancy. Already three decades ago, Herrero et al. (1992) report that evolutionary masses are systematically larger

Downloaded from https://academic.oup.com/mnras/article/499/2/1918/5905414 by guest on 11 February 2026

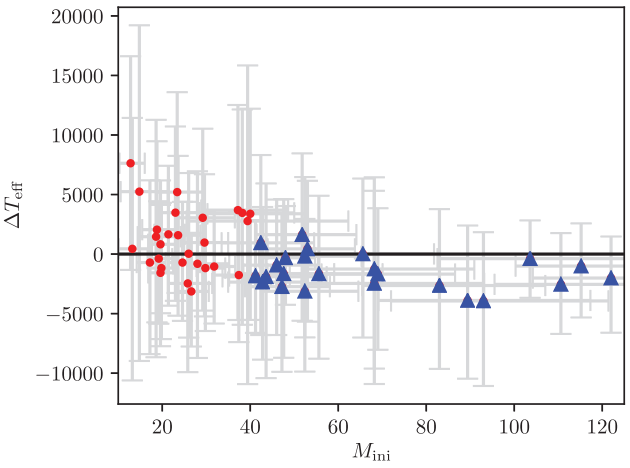


Figure 5. Spectroscopic minus evolutionary temperature against initial stellar mass (red dots). Stars with initial mass >40 $M_\odot$ are shown as blue triangles. Evolutionary temperatures are systematically larger for stars more massive than $\sim 40\,M_\odot$.

than spectroscopic masses. However, our sample does not allow us to draw any conclusion on the negative mass discrepancy. Stars with $M_{\rm ini} > 80\,M_\odot$ the gravities agree and no systematic trend is visible.

The only other variable quantity, which goes into the calculation of the spectroscopic mass, is the stellar radius, which is defined by the luminosity and temperature ($M \propto gR^2 \propto gL/T^4$). We compared the spectroscopic luminosities with those with the highest probability by BONNSAI (mode of PDF) and found a systematic offset of −0.08 dex (Fig. S8). For the given set of stellar parameters stellar evolution models systematically under-predict the stellar luminosity, which leads to a lower evolutionary mass. However, the systematic occurs over the whole mass and luminosity range.

The picture is different for the temperature (Fig. 5). The temperatures of stars with $M_{\rm ini} > 40\,M_\odot$ are systematically overpredicted by the evolutionary models. This could be a result of the stellar wind of the most massive stars. The outer boundary in stellar structure calculations is approximated by a plane–parallel grey atmosphere without wind. The effect of wind blanketing is neglected as well, which alters the temperature and ionization structure of the stellar atmosphere (Hummer 1982; Kudritzki et al. 1989). The mass-loss rate is only a parameter, which removes mass from the star. With increase in stellar mass and luminosity the mass-loss rates increase as well and the stellar wind becomes more and more optically thick. The photosphere which is defined at an optical depth of $\tau = 2/3$ gradually shifts into the stellar winds and is then also referred as a pseudo-photosphere. A comparison with plane–parallel stellar atmosphere models without winds computed with CMFGEN showed that this temperature offset for those stars in our sample is between a few hundred to around 1000 K, which is well within the temperature uncertainties. This discrepancy largely depends on the β exponent of the velocity law rather than the mass-loss rate. The strong dependence on the temperature might explain the discrepancy between spectroscopic and evolutionary masses for stars with ($M_{\rm ini} \gtrsim 80\,M_\odot$), where spectroscopic and evolutionary gravities largely agree.

By considering only stars with masses greater than $80\,M_\odot$, we investigate how these systematics add up. For those objects, the average mass ratio of $M_{\rm spec}/M_{\rm evo} = 1.52$. The average $g_{\rm spec}/g_{\rm evo} = 1.04$, $L_{\rm spec}/L_{\rm evo} = 1.01$, and $(T_{\rm evo}/T_{\rm spec})^4 = 1.20$, which leads to $M_{\rm spec}/M_{\rm evo} = 1.27$. The systematics described above can only partially explain the observed positive mass discrepancy. We conclude that the high spectroscopic masses cannot be reproduced by current stellar models. Relevant physics might be not included or not well enough understood. However, mixing or binary mass transfer would even increase the mass discrepancy as it would lead to even lower evolutionary masses.

To summarize, BONNSAI systematically under-predicts L over the whole mass range. The temperatures for the most massive stars ($\gtrsim$40 $M_\odot$) are overpredicted while gravities are overpredicted for stars less massive than $\sim 80\,M_\odot$. The shift to higher temperatures and gravities can also implicate younger ages. At luminosities above $\log L/L_\odot \sim 5$, the isochrones fan out and changes in the temperature are less critical on the resulting age (Fig. 2). The systematics could be a result that star occupied different location in the HRD for a different period of time. This information is provided to BONNSAI by the evolutionary tracks which are evaluated when determining e.g. stellar masses and ages for given sets of observables. As our uncertainties are rather large, the probability where a star is most likely to be located in the HRD becomes more relevant. By looking at the predicted HRD by BONNSAI most stars are placed near the ZAMS, where they also spend most of the time during their main-sequence (MS) lifetime (Fig. S3).

The positive mass discrepancy between spectroscopic and evolutionary masses was already observed in Galactic O-type stars ($\gtrsim 35\,M_\odot$) by Markova, Puls & Langer (2018). Markova et al. (2018) compared the spectroscopic with the derived evolutionary masses using the BONN (Brott et al. 2011) and GENEVA (Ekström et al. 2012) evolutionary tracks. The mass discrepancy is more pronounced for masses based on the GENEVA tracks. In our analysis, we used the BONN tracks with LMC composition and find a clear trend towards larger evolutionary masses $\gtrsim 40\,M_\odot$. Markova et al. (2018) proposed that the positive mass discrepancy can be explained in terms of overestimated mass-loss rates in evolutionary model calculations on the basis of the Vink et al. (2000, 2001) mass-loss prescriptions. Based on the physical properties of the individual components of spectroscopic-eclipsing binary system HD 166734 and their N-abundance ratio (Mahy et al. 2017), Higgins & Vink (2019) excluded mass-loss rates which lie outside 0.5–1.5 times the Vink et al. (2000, 2001) mass-loss prescription. In addition, rotational mixing is necessary and they favoured larger overshooting parameters of the order of $\alpha = 0.5$ compared to the BONN $\alpha = 0.335$ and GENEVA $\alpha = 0.1$ evolutionary models.

4.3 Stellar winds

The usual wind-momentum rate is given by the product of mass-loss rate and terminal wind velocity ($\dot{M}\upsilon_\infty$). Kudritzki, Lennon & Puls (1995) introduced the modified wind-momentum ($\dot{M}\upsilon_\infty\sqrt{R}$). The latter is expected to be nearly independent of stellar mass and to primarily depend on the stellar luminosity for fixed metallicity (for more details see Puls et al. 1996). The modified WLR relation allows us to compare the wind properties of population of hot massive stars.

Fig. 6 shows the WLR for our sample. We assumed an unclumped, homogeneous wind (i.e. $f_{\rm V} = 1.0$). Mass-loss rates of the three WNh stars were corrected accordingly to their adopted $f_{\rm V} = 0.1$ ($\dot{M}/\sqrt{f_{\rm V}}$). We excluded stars which had no υ_∞ measurement in Paper I. We derived an observed WLR of the form $\log(\dot{M}/\sqrt{f_{\rm v}}\upsilon_\infty\sqrt{R/R_\odot}) = m_0 \log(L/L_\odot) + C_0$ with coefficients m_0 and C_0 given in Table 2. Fits through all and apparent single stars marginal diverge. The

Downloaded from https://academic.oup.com/mnras/article/499/2/1918/5905414 by guest on 11 February 2026

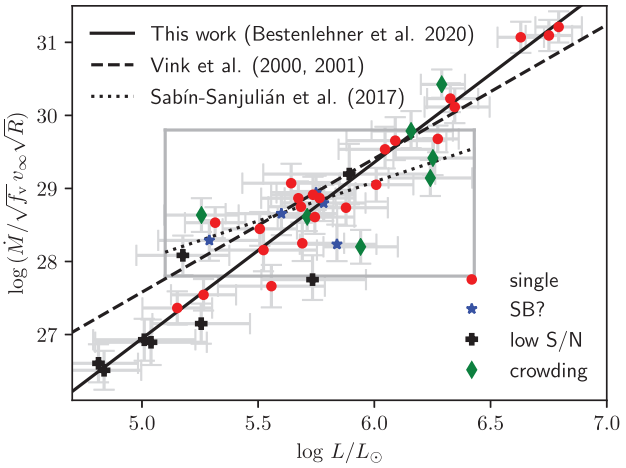


Figure 6. WLR relation. Black solid line is a linear fit through our sample. The theoretical prediction by Vink et al. (2000, 2001) is shown as black dashed line. We indicated the empirical found by Sabín-Sanjulián et al. (2017) as black dotted line while the grey lined box marks the parameter space of their study.

black solid line is an orthogonal-distance regression fit through our data considering abscissa and ordinate errors.[2] The WLR covers a luminosity range of 2 dex from faint late O stars with weak winds up to the extremely bright WNh stars with optically thick winds. The theoretical prediction by Vink et al. (2000, 2001) is less steep than found empirically. Predicted mass-loss rates are higher at the low luminosity end, while for the three WNh stars they are lower. Taking into account the observed wind inhomogeneity of $f_v \sim 0.1$ for WNh stars, the mass-loss prediction is in good agreement, even though the mass-loss prescription was based on models with $4.5 \geq \log L/L_\odot \geq 6.25$. If we assume a similar clumping factor for the O stars, which is supported by radiation-hydrodynamical models including the line-deshadowing instability (Sundqvist & Puls 2018), the predicted mass-loss rates for O stars would be still higher. Another cause for clumping might be the result of subsurface convection (Cantiello et al. 2009).

A volume filling factor $f_v \sim 0.1$ is also supported by Bestenlehner (2020). The author derived a mass-loss recipe which predicts how the mass-loss rate scales with metallicity and at which Eddington parameter (Γ_e, considering only the electron scattering opacity) the transition from optically thin O star to optically thick WNh star winds occurs. With the definition of the transition mass-loss rate, introduced by Vink & Gräfener (2012), Bestenlehner (2020) was able to calibrate the absolute mass-loss rate scale for the chemical composition of the Tarantula Nebula and obtained a volume filling factor $f_V = 0.23^{+0.40}_{-0.15}$ for the sample studied here.

In the context of VFTS, Ramírez-Agudelo et al. (2017) report for the O giants/supergiants a WLR slope in agreement with the prediction by Vink et al. (2000, 2001), while Bestenlehner et al. (2014) note a less steep slope for the most luminous O-type stars ($\log L/L_\odot > 5.5$, Table 2). Sabín-Sanjulián et al. (2017) found in their sample of O dwarfs an even shallower WLR for stars with $\log L/L_\odot > 5.1$ (black dotted line). In the grey box, we indicate the parameter space of the stars by Sabín-Sanjulián et al. (2017). Interestingly, in this parameter range our WLR is less tight. Our targets inside the grey box seem to follow the WLR by Sabín-Sanjulián et al. (2017) and we are able to confirm their findings by considering only stars which lie in their parameter space. For the most massive and luminous objects with a high mass-loss rate and optically thick winds, the steeper slope could be the result of the increasing efficiency of multiline (ML) scattering in dense stellar winds (Friend & Castor 1983; Puls 1987; Lucy & Abbott 1993), which might increase $\dot{M}$ significantly (factors of up to ∼3 are not unlikely) compared to the O star winds. On the low luminosity side, we might begin to see the weak-wind domain (e.g. Puls, Vink & Najarro 2008), which gives rise to lower than predicted $\dot{M}$ and also a steeper slope towards standard conditions. On one hand, the most luminous stars with ML scattering and on the other hand the less luminous stars in the potential weak-wind domain result in an overall steeper WLR slope than expected and relative to the conditions in the grey rectangle.

Mass-loss rates from objects with weak winds can be uncertain derived from optical spectra. A future study of the stellar wind parameters including UV diagnostics will be presented in Paper IV.

4.4 Comparison with previous studies

Massey & Hunter (1998) and de Koter et al. (1998) used the Faint Object Spectrograph (FOS) and the Goddard High Resolution Spectrograph (GHRS) aboard of *HST* to obtain UV and optical spectra of individual stars in and around R136. More recently, Crowther et al. (2010) combined those archival data with near-IR VLT/SINFONI spectra plus VLT/MAD *K*-band photometry to perform a multiwavelength spectroscopic analysis. These studies derived temperatures and luminosities and estimated initial stellar masses using evolutionary models. A summary of stellar parameters of stars in common with our study is given in Table S1.

From *HST*/FOS spectra, Massey & Hunter (1998) estimated properties of 11 stars in common using two different spectral type – temperature scales. The absolute bolometric magnitudes $M_{\rm bol}$ based on the temperature scale by Vacca, Garmany & Shull (1996) are in better agreement with our results and only listed in Table S1. The temperature scale was based on unblanketed stellar atmosphere models, which results in 2000–8000 K higher temperatures and 0.2–0.35 dex higher luminosities estimates (Martins, Schaerer & Hillier 2005). As a result of this, luminosities are in agreement with our results within +0.2 dex. The only exceptions are H36 and H46 which are in our spectroscopic analysis around 0.4 dex more luminous. The reason for this agreement might be that our luminosity scale is anchored on *K*-band photometry leading to systematically higher *L* while Massey & Hunter (1998) relied on optical WFPC2 photometry which are more affected by extinction, even though they determined extinction parameters. Estimated initial masses agree reasonable well up to ∼ 100 $M_\odot$ but are systematically lower at higher masses (Table S1). Massey & Hunter (1998) used the evolutionary models by Schaerer et al. (1993) extending up to 120 $M_\odot$ which were extrapolated for more luminous and massive stars.

11 stars are in common with de Koter et al. (1997, 1998). They used the ISA-WIND non-LTE model atmosphere code (de Koter, Schmutz & Lamers 1993) to derive temperature and mass-loss rates from *HST*/FOS and *HST*/GHRS data. Their temperatures are systematically lower than ours and result in lower luminosities (Table S1). Evolutionary models from Meynet et al. (1994) extending to 120 $M_\odot$ were applied to estimate the initial masses. The most massive star in their sample is R136a1, $M_{\rm ini} = 120\,M_\odot$, which has according to our analysis $M_{\rm ini} = 250\,M_\odot$. With decreasing luminosities, differences become small and H55 agrees well with our results (Table S1).

[2]In many other studies, a more conventional regression is done considering only errors in the modified wind momentum rate, see discussion in Markova et al. (2004).

Downloaded from https://academic.oup.com/mnras/article/499/2/1918/5905414 by guest on 11 February 2026

Table 2. Coefficients for WLR of the form $\log(\dot{M}/\sqrt{f_v}\upsilon_\infty\sqrt{R/R_\odot}) = m_0 \log(L/L_\odot) + C_0$. Coefficients listed below the horizontal line are not shown in Fig. 6 and are given for reference.

	m_0	C_0	Source
All stars	2.41 ± 0.13	14.88 ± 0.74	Fig. 6
LMC prediction	1.83 ± 0.04	18.43 ± 0.26	Vink et al. (2000), Vink et al. (2001)
VFTS O dwarfs	1.07 ± 0.18	22.67 ± 0.99	Sabín-Sanjulián et al. (2017)
Apparent single stars	2.34 ± 0.13	15.37 ± 0.75	This study
VFTS O giants/supergiants	1.78 ± 0.14	19.17 ± 0.79	Ramírez-Agudelo et al. (2017)
VFTS O stars ($\log L/L_\odot > 5.5$)	1.45 ± 0.16	20.70 ± 0.88	Bestenlehner et al. (2014)

Crowther et al. (2010) spectroscopically analysed the four brightest stars in R136 combining *HST*/GHRS, *HST*/FOS, and VLT/SINFONI data. There is an overlap of three stars with our sample. For the stars in common they derived systematically higher temperatures, in particular for R136a1 where $\Delta T_{\rm eff} \approx 7000$ K (Table S1). In the hotter model, the N V λ4604 and 4620 lines are too strong. The N-abundance can be reduced to match the line intensity, but N IV λ4058 would be then too weak. As R136a1 shows an enriched He composition at the surface a reduced N-abundances would also contradict the findings by Rivero González et al. (2012b) and Grin et al. (2017) that the same process should be responsible to bring up both materials to the surface. Our luminosity for R136a1 is 0.15 dex lower while R136a2 and R136a3 agree within 0.05 dex. The initial masses were derived with evolutionary models published later in Yusof et al. (2013) extending up to 500 $M_\odot$. Initial masses agree within their uncertainties, but with the largest discrepancy for R136a1. Crowther et al. (2010) obtained 320^{+100}_{-40} $M_\odot$ and we derive 251^{+50}_{-35} $M_\odot$ which is a result of the large difference of the determined effective temperature.

5 DISCUSSION

5.1 Helium enrichment: mixing or mass-loss?

In this section, we discuss the surface helium enrichment and HRD position. To simultaneously explain the observed He-abundance and HRD location of the star, we require enhanced mixing due to rotational mixing or high enough mass-loss rates to shed away the outer hydrogen layers to uncover the helium rich layers.

Fig. 7 shows the helium mass fraction (Y) against the line broadening. The quality of our data does not allow us to disentangle projected rotational velocity and macroturbulent velocity (Section 3.1). Therefore, the projected rotational velocities stated on the abscissa are upper limits of the actual $\upsilon \sin i$. In agreement with Bestenlehner et al. (2014), Y does not correlated with $\upsilon \sin i_{\rm max}$, which is an indication that rotational mixing might be not the dominant process for the helium enrichment at the stellar surface.

With the exception of the WNh stars, evolutionary models are able to reproduce helium composition and HRD location of the O-type stars without the necessity of high rotation rates. With blue triangles, we indicated the predicted current rotation rates by BONNSAI of the WNh stars. These stars have a most probable rotation rate of 250 km s^{-1} excluding essentially lower rotation rates. Through projection effects lower $\upsilon \sin i$ values can be observed and we cannot exclude that our WNh star actually rotate much faster as the inclination is unknown (Fig. 8). However, the 11 helium enriched Of/WN and WNh stars of Bestenlehner et al. (2014) also do not show high $\upsilon \sin i$ values. The stellar models by Köhler et al. (2015), which fit L, $T_{\rm eff}$, and Y, evolve chemically homogeneously due to rotational mixing and reproduce those stellar parameters at about the same time (∼1.2 Myr, Fig. S9).

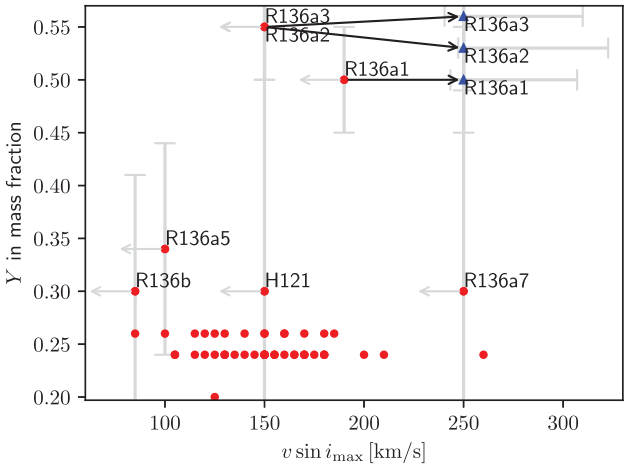


Figure 7. Surface helium abundances versus upper limits of the projected rotation (red dots and arrows pointing to the left). There is no clear correlation between $\upsilon \sin i_{\rm max}$ and Y. Blue triangles indicated the most probable current day rotation rates for the three WNh stars, which largely excludes $\upsilon_{\rm rot} <$ 250 km s^{-1}.

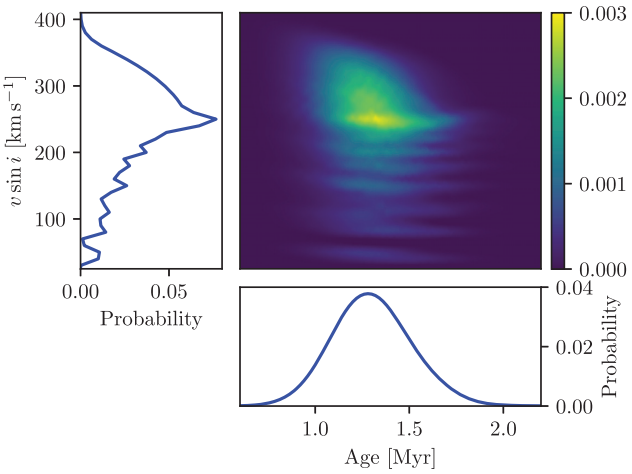


Figure 8. R136a3: probability distributions for stellar age and current projected-rotational velocity ($\upsilon \sin i$). We assumed a flat prior distribution for $\upsilon \sin i$. The most probable projected rotational velocity is ∼250 km s^{-1}. The stellar age is well constrained.

In Fig. 8, we visualize the probability distributions of R136a3 with the largest joint Y for stellar age and current projected rotational velocity provided by BONNSAI assuming a flat $\upsilon_{\rm rot}$ prior. $\upsilon \sin i_{\rm max}$

Downloaded from https://academic.oup.com/mnras/article/499/2/1918/5905414 by guest on 11 February 2026

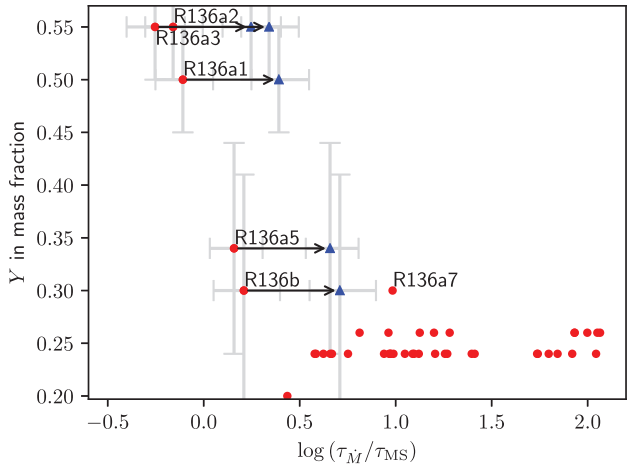


Figure 9. Surface helium abundances versus mass-loss time-scale for homogeneous (red dots) and clumped winds (blue triangles) over main-sequence lifetime. Main-sequence lifetimes are estimated based on the most probable initial mass according to the models of Brott et al. (2011) and Köhler et al. (2015).

of R136a3 is ∼150 km s^{-1} and in the 2σ confidence range of the most probable $\upsilon \sin i = 250^{+80}_{-55}$ km s^{-1} from Fig. 8. Its surface abundance Y and age of R136a3 is well determined at around 1.3 Myr. An older age or flat PDF extending to older ages could have provided a probability that the star might have spun down and transported the helium enriched material from the core to the surface on a longer time-scale. There is one exception which might be chemically enriched due to rotational mixing. R136a7 shows a helium enriched chemical composition and has one of the highest upper limits for $\upsilon \sin i_{\max}$. This could be interpreted as R136a7 being a mass gainer or merger product but the uncertainties on Y are large.

All helium enriched stars ($Y \geq 0.3$) have in common that they show emission-line features in their spectra indicating high $\dot{M}$. Herrero & Lennon (2004) and Vink (2015) proposed that $\dot{M}$ dominates the evolution for stars above 60 M$_\odot$. Bestenlehner et al. (2014) studied Y at the stellar surface as a function of mass-loss rate over stellar mass ($\dot{M}/M$), which can be interpreted as the inverse mass-loss time-scale ($\tau_{\dot{M}}$). They found that for $\log \dot{M}/M \gtrsim -6.5$ there is a well-defined correlation between Y and $\dot{M}/M$ when the mass-loss time-scale ($\tau_{\dot{M}} \lesssim 3$ Myr) is comparable to the main-sequence lifetime. In agreement with Bestenlehner et al. (2014), we find a similar correlation for $\log \dot{M}/M \gtrsim -6.7$ (Fig. S10), but we take it a step further. Based on the initial masses given by BONNSAI, we estimated the main-sequence lifetime (τ_{MS}) according to Brott et al. (2011) and Köhler et al. (2015) and examine the helium enrichment as a function of $\tau_{\dot{M}}/\tau_{MS}$.

Fig. 9 shows Y versus $\tau_{\dot{M}}/\tau_{MS}$. Only the three WNh stars have shorter mass-loss time-scale than MS lifetime, even though the MS lifetime decreases with increasing stellar mass. We find a correlation of Y with $\tau_{\dot{M}}/\tau_{MS}$ at $\log(\tau_{\dot{M}}/\tau_{MS}) \lesssim 0.2$ (red dots in Fig. 9). A star evolves quasi-chemical homogeneously when $\tau_{\dot{M}} < \tau_{MS}$ because the MS lifetime corresponds to the nuclear fusion time-scale of hydrogen in the core. However, if we account for wind inhomogeneity and correct the mass-loss rates for a volume filling factor $f_V = 0.1$ derived from the electron scattering wings of the emission-line stars, $\tau_{\dot{M}}$ increases by factor of $\sqrt{10}$ or 0.5 dex (blue triangles in Fig. 9). The correlation already occurs at $\log \tau_{\dot{M}}/\tau_{MS} \lesssim 0.7$ near the location of R136b. After considering the wind inhomogeneity no star has $\tau_{\dot{M}} < \tau_{MS}$ and evolves virtually chemical homogeneously.

R136a3 has the smallest $\tau_{\dot{M}}/\tau_{MS}$ ratio and has already lost 25 per cent of its initial mass. The observed $Y = 0.55$ might be produced by mass-loss only, but the mass-loss rates would need to be significantly increased, which is not really justified (Section 4.3). A much higher mass-loss rate would not only mean a much higher initial mass but also the star would spin-down on very short time-scale and low υ_{rot} would be expected. Fig. 7 shows that this is not the case, in particular for R136a1. $\dot{M}$ steeply increases when the star approaches the Eddington limit (e.g. Gräfener & Hamann 2008; Gräfener et al. 2011; Vink et al. 2011; Bestenlehner et al. 2014; Bestenlehner 2020). A period of extensive mass-loss at the beginning of the evolution of VMS might help to solve the current tension (e.g. Bestenlehner et al. 2014; Schneider et al. 2018b).

Vink et al. (2010), Castro et al. (2014), and McEvoy et al. (2015) suggested additional core overshooting for massive stars to bring the predicted location of the terminal-age main-sequence (TAMS) by Brott et al. (2011) in agreement with the observations. With increasing stellar mass the convective core increases as well. The WNh stars in access of 100 M$_\odot$ are largely convective and the amount of core overshooting might be less relevant. Higgins & Vink (2019) reported that the nitrogen compositions of the binary HD 166734 consisting of two O supergiants with masses between 30 and 40 M$_\odot$ could not be reproduced by mass-loss and core overshooting alone. At least some amount of rational mixing is necessary to transport the right amount of nitrogen to the surface to match the observed compositions of both stars. Rivero González et al. (2012b) and Grin et al. (2017) found a correlation between He and N enrichment suggesting that the same process should be responsible to dredge-up both elements.

Chemically homogeneously evolving models due to rotational mixing well reproduce the observed L, T_{eff}, and Y of the WNh stars. All the stars need relatively fast initial rotation in excess of 300 km s^{-1}. Such fast rotation is not found at lower masses in 30 Doradus and appears to be in conflict (Schneider et al. 2018b). Stellar models with enhanced mixing predict lower evolutionary masses, which might be the reason for the observed positive mass discrepancy in Section 4.2. However, only the WNh stars, where we were not able to derive M_{spec}, require high initial υ_{rot} to reproduce the observables. This might be an indication that some physical conditions are not well enough understood or missing. We can conclude that the evolution of the most massive is dominated by mass-loss, as seen by the tight correlation in Figs 9 and S10. Therefore, we do not expect a correlation of Y with $\upsilon \sin i_{\max}$ which is supported by Fig. 7, but an additional mixing process such as rotational mixing or other mixing process appears to be still necessary to reproduce the observables.

5.2 Cluster ages of R136

In Fig. 10, we show the probability density functions of ages. This shows a young stellar population up to 2.5 Myr (38 stars) and an older population extending beyond 2.5 Myr (17 stars). Most but not all of the older objects have a low S/N spectrum. We found a median age around 1.6 Myr of R136, similar to what had been found in Paper I from UV calibrations. Based on pre-MS stars and their associated tracks, Cignoni et al. (2015) established that the star formation rate in R136 peaked between 1 and 2 Myr. Sabbi et al. (2012) identified a slightly older group located ∼5.4 pc to the north-east potentially merging into R136. Their analysis suggests that the majority of stars in the north-east clump were formed between 2 and 5 Myr ago while R136 is not older than ∼2 Myr.

Fig. 11 indicates that the older population (>2.5 Myr) representing 1/3 of the stars is spatially well distributed within 0.5 pc of R136.

Downloaded from https://academic.oup.com/mnras/article/499/2/1918/5905414 by guest on 11 February 2026

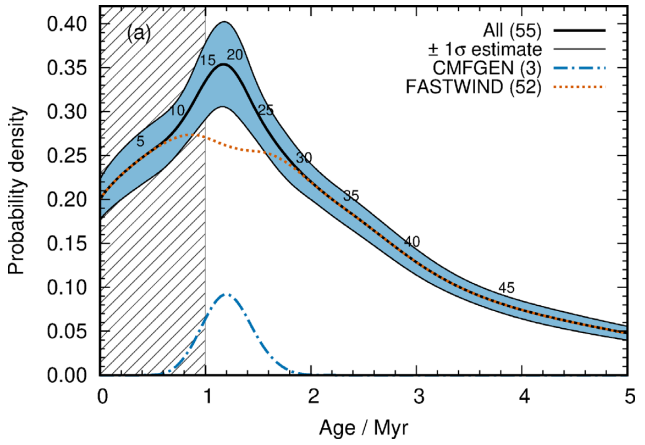


Figure 10. Probability density functions of stellar ages (black solid line and $\pm 1\sigma$ estimate blue shaded). Blue dot–dashed line: PDF of stars analysed with CMFGEN. Red dotted line: PDF of stars analysed with FASTWIND. Numbers are cumulative counts. The population of R136 can be roughly divided into two, a younger one with an age <2.5 Myr and an older population with an age >2.5 Myr. Hatched area corresponds to the minimum age R136 of 1 Myr.

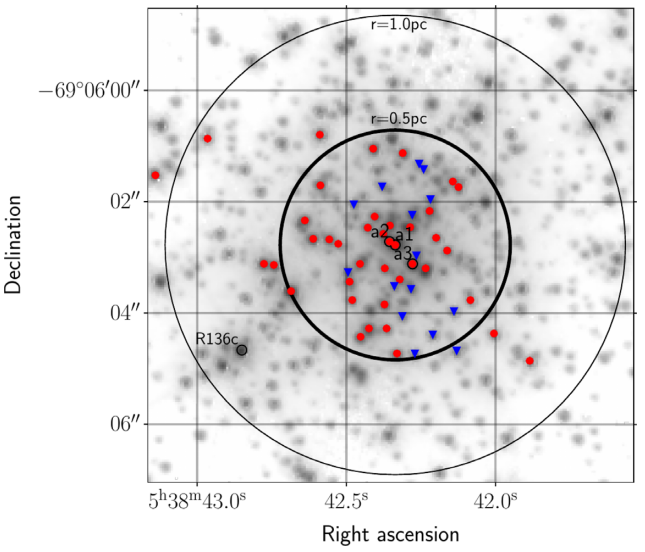


Figure 11. Spatial distribution of our targets in R136. Stars indicated by a red dot likely belong to a younger population while blue triangles to an older ($\gtrsim$2.5 Myr). The position of older and younger stars is randomly distributed. Black bold solid circle of radius 0.5 pc and black solid circle of radius 1.0 pc are centred on R136a1. The background image was taken with *HST*/WFC3 using the *F555W* filter.

R136 is located in an extended H II region NGC 2070, which contributes to the projected stellar population of R136. Hénault-Brunet et al. (2012) find that this contribution is $\lesssim$5 per cent in the inner 1.25 pc corresponding to only $\lesssim$3 stars. If this older population is part of a more diffuse surrounding population, it should become more dominant when moving out to larger radii.

If those stars are descended from the north-east clump, their number is still rather large and a noticeable overdensity of older stars should be found in the proximity to R136. Castro et al. (2018) observed the surrounding region centred on R136 with Multi Unit Spectroscopic Explorer (MUSE) on the Very Large Telescope. The four field mosaic covers a box of $\sim$30 pc $\times$ 30 pc and the spectroscopic analysis of Castro et al. (in preparation) might confirm

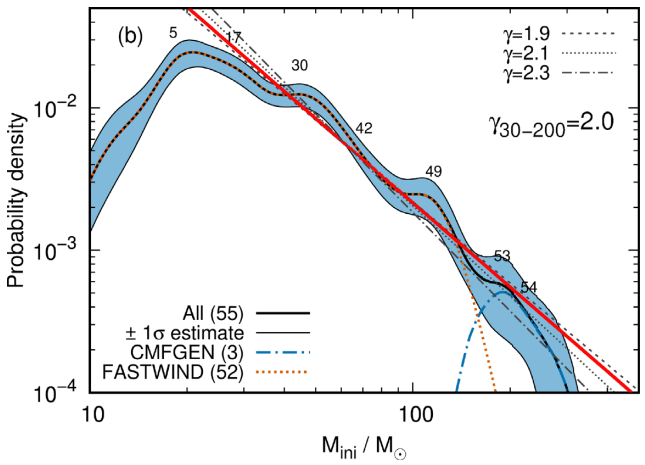


Figure 12. Probability density functions of initial stellar masses. Results are indicated as in Fig. 11. Red solid line is the best fit with slope $\gamma \approx 2$ derived over the 30–200 mass range. Slopes of $\gamma = 1.9$, 2.1, and 2.3 seemed to work similarly well (grey dashed, dotted, and dot–dashed lines). Our sample is complete down to 30–40 $M_\odot$. Seven stars are more massive than 100 $M_\odot$.

the older foreground population or the north-east clump merging into R136. Currently, we are not able to establish if the apparently older stars originated from the north-east clump, an older foreground population due to the three-dimensional nature of 30 Doradus, or that R136 consists of a multiple age population.

The age PDF, black solid line in Fig. 10, culminates at $\sim$ 1.2 Myr suggesting that the star formation rate in R136 peaked at around this time. The prominent peak is mainly caused by the three most massive WNh stars (blue dash–dotted line) while the O star distribution (orange dotted line) is flatter suggesting a more continuous star formation rate up to 2 Myr or larger age errors.

Considering the surface helium mass fraction of the three WNh stars R136a1, a2, and a3, we can estimate a lower age boundary for R136. The helium shown at the surface has to be produced in the core first due to nuclear fusion. As probably more helium has been produced than visible at the surface this boundary is a lower limit. Under these assumptions R136 must be older than 1.0 Myr which is indicated as the hatched area in Fig. 10. Lennon et al. (2018) report that the proper motion of VFTS 016 is consistent with an ejection from R136. If VFTS 016 is ejected from R136 during or shortly after the cluster was formed, it would set a lower age limit of 1.3 Myr based on its current distance to R136 and proper motion.

Even though our sample contains stars with ages up to $\lesssim$6 Myr, the majority of stars in R136 has an age between 1 and 2 Myr. Based on the minimum age of 1.0 Myr using *Y*, the lower age limit of 1.3 Myr by dynamical ejection of VFTS 016 and the distribution of the PDF we can assume a cluster age of R136 between 1.0 and 2.0 Myr.

5.3 Initial mass function and upper mass limit

In Fig. 12, we show the IMF of R136. Our sample is complete down to 30–40 $M_\odot$, which largely represents the stars younger than 2.5 Myr (Fig. 10). Similar to Schneider et al. (2018a), we assumed a power-law function of the form $\xi(M) \propto M^{-\gamma}$ with the stellar mass (M) and exponent γ to fit the slope of the IMF. To accurately determine the slope of the IMF, it is crucial to know down to which stellar mass the sample is complete, or alternatively the completeness of a given mass bin. We fitted power laws over the mass range 30–200 $M_\odot$ to the distribution of initial masses. The best fit is indicated as a red

Downloaded from https://academic.oup.com/mnras/article/499/2/1918/5905414 by guest on 11 February 2026

line in Fig. 12 and has an exponent $\gamma = 2.0 \pm 0.3$. Slopes of $\gamma = 1.9$, 2.1, and 2.3 seemed to work similarly well (grey dashed, dotted, and dot–dashed lines). All IMFs show a clear change in slope at $M \lesssim 30\,M_\odot$. On the one hand this may reflect incompleteness in this mass regime. We removed two SB2s (H42 and H77) from our sample which would add four stars to the mass range between 30 and 40 $M_\odot$ based on the estimated properties from Paper I assuming equal mass binaries and similar stellar parameters suggested from their optical spectral types. On the other hand it may point to R136 being a composite of stellar population.

Schneider et al. (2018a) derived $\gamma \approx 1.90^{+0.37}_{-0.26}$ for a stellar sample in the wider 30 Doradus region which is complete down to 15 $M_\odot$. Our slope is in line with theirs, but the uncertainties are significantly larger. For the solar neighbourhood, Salpeter (1955) obtained a slope of $\gamma \approx 2.35$ from stellar populations with masses up to 17 $M_\odot$ (B0V star). The most common IMFs to simulate and interpret clusters and galaxies are Kroupa (2001) and Chabrier (2003). Both studies suggest a $\gamma \approx 2.3$. A shallower slope at the high-mass end would predict more massive stars. However, the uncertainties in our analysis are too large to firmly suggest this.

Seven stars have initial masses above 100 $M_\odot$. Three of them are more massive than 150 $M_\odot$ with the most massive two exceeding 200 $M_\odot$. Figer (2005) proposed a canonical upper mass limit of $\sim 150\,M_\odot$, which is challenged by these findings. If we include R136c (alias VFTS 1025; Bestenlehner et al. 2014; Schneider et al. 2018a) as a cluster member, we find that three stars in R136 exceed 200 $M_\odot$. The upper mass limit might still be valid if those VMSs are stellar merger products (Banerjee et al. 2012), although all would need to be have merged within 1–2 Myr after formation. Banerjee et al. (2012) simulated a handful of clusters with identical initial conditions. Even though none of their simulations is able to predict these numbers, we cannot exclude the merger scenario, as results considerably varied between their simulations.

VFTS 682 is a VMS in apparent isolation with a current day mass $\sim 150\,M_\odot$ (Bestenlehner et al. 2011). It is a candidate runaway star from R136 (Renzo et al. 2019). This supports the existence of VMSs $> 150\,M_\odot$ in general and in particular in the core of R136. Tehrani et al. (2019) discovered that Mk34 is likely the most massive binary system known today, and is located just to the east of R136 with a projected distance of ~ 3 pc. Mk34 consists of two WN5h stars showing a similar spectrum to VFTS 682. The combined mass of the system exceeds 250 $M_\odot$. Even though most stars are found in binaries or higher order systems (Sana et al. 2012, 2013; Maíz Apellániz et al. 2019), it is still possible that in some rare cases a system like Mk34 merged during the formation process or on the MS and formed a single VMS exceeding 200 $M_\odot$.

Even though the uncertainties are large, there is no clear evidence from the IMF of Fig. 12 that the most massive stars are stellar mergers. Based on the most massive stars in R136, NGC 3603 and the Arches Cluster (Crowther et al. 2010) revised the upper mass limit. Bestenlehner (2020) finds that the mass-loss rates of the most massive stars might be underestimated by a factor of ∼2 in the BONN models. This could mean that the actual initial masses of those stars are even larger suggesting a higher upper mass limit. It has been suggested that the first stars in the Universe had masses in excess of 1000 $M_\odot$ (e.g. Bromm, Coppi & Larson 1999). Based on Monte Carlo radiative transfer models, Vink (2018) proposed a metallicity-dependent upper mass limit with higher stellar masses in metal poorer environments. With the current number and properties of known VMS in spatially resolved clusters in the Milky Way and Magellanic Clouds it is difficult to find an indisputable answer to the question of the upper mass limit of stars.

5.4 Ionizing fluxes and mechanical feedback

In this section, we compare our integrated ionizing fluxes and mechanical feedback with Doran et al. (2013). The ionizing flux (Q_0) is measured in photons per second (ph s^{-1}) while the mechanical feedback is given by the stellar wind luminosity ($L_{SW} = \frac{1}{2}\dot{M}\upsilon_\infty^2$) in erg s^{-1}. Doran et al. (2013) applied a template method to estimate the stellar parameters and used theoretical mass-loss predictions by Vink et al. (2001) to evaluate $\dot{M}$. They assigned typical υ_∞ values based on averaged values by Prinja, Barlow & Howarth (1990). Doran et al. (2013) estimated the ionizing and mechanical output for the entire Tarantula Nebula within a radius of 150 pc around R136a1 and emphasized that the few most massive and luminous stars dominate the overall ionizing and mechanical budget of 30 Doradus. In this work, we calculated the mechanical feedback with the values given in Table 1 where we explicitly list the ionizing fluxes.

Fig. 11 shows that our sample is likely complete in terms of stars contributing to the cumulative Q_0 and L_{sw} within a radius of 0.5 pc around R136a1. We derived an integrated $\log Q_0$ [ph/s] = 51.44 and L_{SW} [erg/s] = 39.07. Doran et al. (2013) obtained an integrated $\log Q_0 = 51.36$ and $\log L_{SW} = 38.58$ using their table D.2. Both results are similar, but we find a 0.5 dex higher stellar wind luminosity. Accounting for a volume filling factor ($f_v = 0.1$), our result would be 0.5 dex lower and in agreement ($\log L_{SW} = 38.57$). Extending the sampled region to 1 pc, we find $\log Q_0 = 51.46$ and $\log L_{SW} = 38.57$ while Doran et al. (2013) find 51.48 and 38.68, respectively. The main contributor in this range is the WN5h star R136c (Bestenlehner et al. 2014), which essentially accounts for the increase in Q_0 and L_{SW} in Doran et al. (2013) and is not in our sample.

In our sample, we have seven VMS with masses greater than 100 $M_\odot$. The VMS accounts for ∼57 per cent of the ionizing flux and ∼90 per cent of the stellar wind luminosity relative to all 55 stars. R136 contributes ∼27 per cent of the overall ionizing flux and ∼19 per cent of the overall mechanical feedback to the Tarantula Nebula. We conclude that the cluster R136 is the major contributor to the stellar feedback in the Tarantula Nebula. We confirm that the ionizing and mechanical feedback is dominated by the most massive stars at the top of the IMF.

5.5 The stellar population of R136 and the Tarantula Nebula

The integrated light of star-forming galaxies is dominated by massive stars (Section 5.4 or e.g. Crowther 2019). The interpretation is based on population synthesis models like STARBURST99 (Leitherer et al. 1999) or BPASS (Eldridge et al. 2017). In this section, we compare the stellar population of R136 (Fig. 13) within a radius of 1 pc and the Tarantula Nebula (Fig. 14) within 150 pc (10 arcmin) from R136a1 (Walborn 1991) to the population synthesis prediction from BPASS (v.2.2.1; Stanway & Eldridge 2018). We downloaded the commonly used and publicly available BPASS output[3] and visualized it with the PYTHON package HOKI that has been designed to interface with the BPASS models and their outputs (Stevance et al. 2020). The publicly available BPASS models for binary population synthesis used the binary, period, and mass distribution according to Sana et al. (2012) and Moe & Di Stefano (2017). Both single and binary models employ in the mass range of our sample, a standard Salpeter (1955) IMF with an exponent $\gamma = 2.35$ and an upper mass limit of 300 $M_\odot$. For more details on the nature of BPASS models, we

[3]https://drive.google.com/drive/folders/1BS2w9hpdaJeul6-YtZum--F4gxWIPYXl

Downloaded from https://academic.oup.com/mnras/article/499/2/1918/5905414 by guest on 11 February 2026

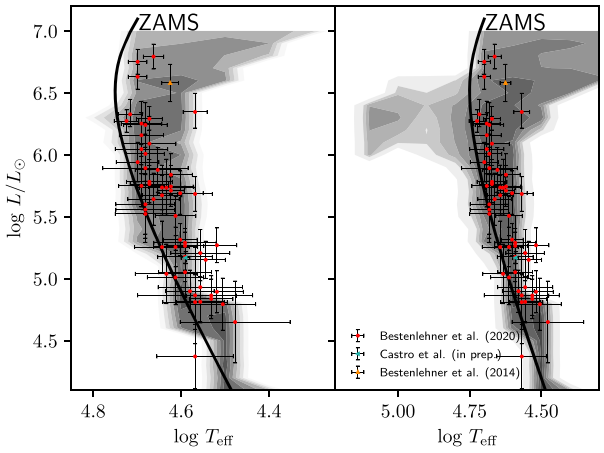


Figure 13. HRD of R136 and overlaid binary population synthesis. The stellar population of R136 within a radius of 1 pc from R136a1 compared to the predicted binary stellar population of an age between 1.0–2.0 (left-hand panel) and 1.0–2.3 Myr (right-hand panel) from BPASS (grey shaded contours; Eldridge et al. 2017; Stevance, Eldridge & Stanway 2020). Each contour represents an order of magnitude difference in stellar number density.

refer the reader to Eldridge et al. (2017) and Stanway & Eldridge (2018).

In the left-hand panel of Fig. 13, we show an HRD of R136 in which we have overlaid the BPASS population synthesis prediction assuming a single starburst from 1 to 2 Myr. The population synthesis contours are truncated at $\log L/L_\odot < 7.0$ corresponding to the upper mass limit of 300 $M_\odot$. Our sample well populate the region near the ZAMS over the whole luminosity range as predicted by BPASS. If we extend the starburst to 2.3 Myr, the first *classical* WR stars become visible to the hot side of the ZAMS (Fig. 13, right-hand panel). Their absence gives us an upper age limit of 2.2 Myr for R136 which confirms our findings from Section 5.2.

Now we consider R136 in the wider context of the Tarantula Nebula. We compiled an HRD of 460 stars using stellar parameters of stars more massive than 15 $M_\odot$ with ages up to ∼12 Myr from the literature (Fig. 14, caption for references). The sample includes apparent single as well as binary stars within 10 arcmin (150 pc) from R136a1 including stars from NGC 2070 and NGC 2060. We overlaid the contours of the BPASS binary population synthesis prediction of a 1–12 Myr old stellar population using the star formation history (SFH) of the Tarantula Nebula by Schneider et al. (2018a). As this SFH is not implemented into BPASS, we divided the age range into 0.02 Myr age bins. The age bins were weighted according to the SFH and stacked. Each contour represents an order of magnitude difference in stellar number density.

A significant number of stars densely populate the region near the ZAMS (∼400), where the BPASS models predicts the highest number densities. The number of around 50 blue supergiants (BSG) is roughly expected based on the BPASS contours. However, only one of those supergiants which is part of a binary system is more luminous than $\log L/L_\odot \gtrsim 5.8$, even though a population of more luminous BSG are predicted. No yellow/red supergiants (Y/RSG) are observed in the Hertzsprung gap between 5000 and 12 000 K. Because only very few are expected due to our sample size, we are not able to quantify an actual disagreement between observation and BPASS prediction. All six RSG are less luminous than $\log L/L_\odot = 5.3$, even though at least a similar number should be observed above this threshold.

Most stars in Fig. 14 have been observed in the context of VFTS (Evans et al. 2011). The selection criterion was a magnitude cut which includes cool stars as well. Any RSG more luminous than $\log L/L_\odot = 5.5$ should have been picked up. However, the observations are in line with the empirical RSG upper luminosity limit of $\log L/L_\odot \approx 5.5$ in the LMC (Davies, Crowther & Beasor 2018), but there total number might be on the lower side.

Turning to the hot side of the ZAMS there are several *classical* WR stars in the Tarantula Nebula around R136 (Fig. 14). Comparing the number densities of WR stars relative to the one near the ZAMS the count of seven WR stars is rather low. At least a factor of 2–3 more WR stars could be expected. Single-star population synthesis models predict that WR stars should be all more luminous than $\log L/L_\odot \gtrsim 5.5$ (Fig. S11). In contrast, the binary synthesis models predict also stars below $\log L/L_\odot < 4.5$, but the shown sample is incomplete below $\log L/L_\odot \sim 5$ on the hot side of the ZAMS. The binary evolution channel seems to be important to form less luminous WR stars or helium stars. A general discussion on the formation of WR stars via binary evolution and the transition between WR and He stars can be found in Shenar et al. (2020).

Based on binary population synthesis models, we find an upper age limit for R136 of 2.2 Myr. Most stars populate the region near and to the cooler side of the ZAMS covering the entire luminosity rage. In the wider context of the Tarantula Nebula, the number of *classical* WR stars is lower than expected based on the BPASS models. We observe a discrepancy between the predicted stellar number densities by BPASS of luminous blue ($\log L/L_\odot \gtrsim 5.8$) and red supergiants ($\log L/L_\odot \gtrsim 5.3$). A potential top-heavy IMF in comparison to the standard Salpeter IMF would increase the discrepancies between number of WR stars and more luminous B/RSG, which is suggested by Schneider et al. (2018a) and this study. This has not only an impact on the predicted radiative and mechanical output of the Tarantula Nebula but also on the analysis and interpretation of unresolved stellar populations in star-forming galaxies.

6 CONCLUSION

In this study, we have spectroscopically analysed 55 stars in R136, the central cluster in the Tarantula Nebula in the LMC. The sample is complete down to about 40 $M_\odot$, including seven VMSs over 100 solar masses. The slope of the WLR is 2.41 ± 0.13 which is steeper than the usually observed value of ∼1.8 (e.g. Mokiem et al. 2007; Ramírez-Agudelo et al. 2017) and predicted value of 1.83 (Vink et al. 2000, 2001) in the LMC.

The most luminous stars ($\log L/L_\odot > 6.3$) are helium enriched at the stellar surface. Luminosities, temperatures, and He-abundances of the three WNh stars are well reproduced by chemically homogeneously evolving stellar models due to rotational mixing. We find a tight correlation of helium surface composition with the ratio of the mass-loss over main-sequence time-scale indicating the importance of mass-loss during their evolution. We conclude that mass-loss dominates the evolution of the most massive stars, but rotational mixing or other mixing processes might be still necessary.

There is an indication that the IMF of massive stars in R136 might be top heavy with a power-law exponent $\gamma \approx 2.0 \pm 0.3$ by comparison to the standard Salpeter exponent, although slopes of 1.9, 2.1, and 2.3 work similarly well due to the large uncertainties. Based on the chemical composition of the most massive stars, we derived a lower age limit of 1.0 Myr for R136. Because there are no *classical* WR stars in our sample of R136, we estimate an upper age

Downloaded from https://academic.oup.com/mnras/article/499/2/1918/5905414 by guest on 11 February 2026

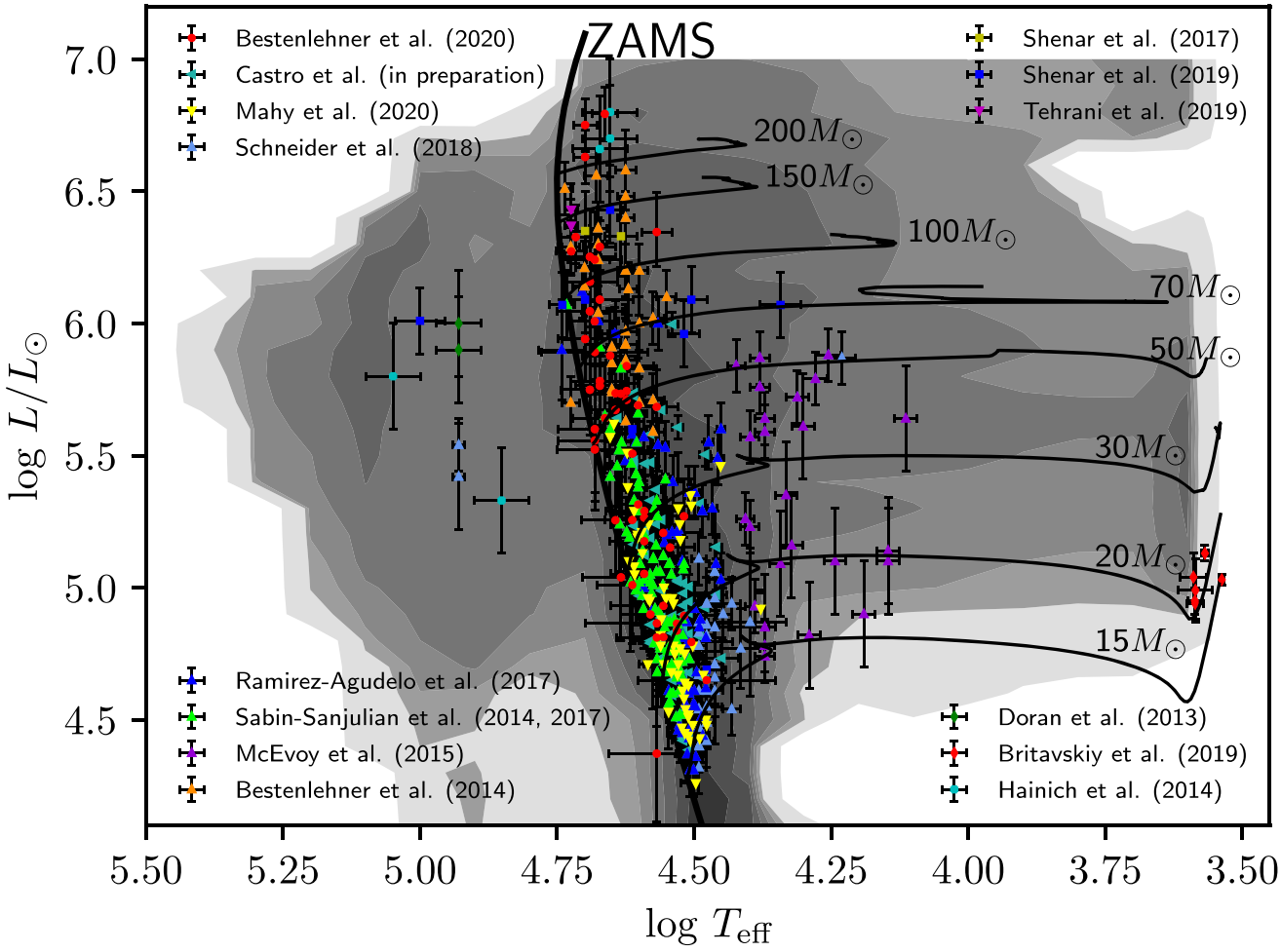


Figure 14. HRD of the Tarantula Nebula and overlaid binary population synthesis. Census of massive stars ($> 15\,M_\odot$) in 30 Doradus in the LMC within a radius of 10 arcmin (150 pc) from R136a1. The age of the observed stellar population is 1–12 Myr (Schneider et al. 2018a). Black solid lines are BONN evolutionary tracks and ZAMS (Brott et al. 2011; Köhler et al. 2015). The grey shaded contours visualize the predicted binary stellar population from BPASS (Eldridge et al. 2017; Stevance et al. 2020) for the observed age range. Each contour represents an order of magnitude difference in stellar number density. The figure includes single and binary stars from this work, Doran et al. (2013), Bestenlehner et al. (2014), Hainich et al. (2014), Sabín-Sanjulián et al. (2014, 2017), McEvoy et al. (2015), Ramírez-Agudelo et al. (2017), Shenar et al. (2017, 2019), Schneider et al. (2018a), Britavskiy et al. (2019), Tehrani et al. (2019), Mahy et al. (2020), and Castro et al. (in preparation).

limit of 2.2 Myr. We conclude that the age of R136 is between 1 and 2 Myr.

Based on evolutionary models, the most massive star R136a1 had an initial mass of $250^{+50}_{-35}\,M_\odot$ and a current day mass of $215^{+45}_{-30}\,M_\odot$. Stars more massive than $40\,M_\odot$ exhibit larger spectroscopic masses than evolutionary masses. This positive mass discrepancy problem was already observed for Milky Way stars at a similar stellar mass ($\gtrsim 35\,M_\odot$; Markova et al. 2018).

The ionizing ($\log Q_0\,[\mathrm{ph/s}] = 51.4$) and mechanical ($\log L_{\rm SW}\,[\mathrm{erg/s}] = 38.6$) output of R136 is dominated by the most massive stars. The seven most massive stars account for $\sim$57 per cent of the ionizing flux and $\sim$90 per cent of the stellar wind luminosity of R136. R136 as a whole contributes around 1/4th of the ionizing flux and around 1/5th of the mechanical feedback to the overall budget of the Tarantula Nebula.

BPASS population synthesis predictions of R136 are in good agreement, which might be the result of the relative young age of R136. In the wider context of the Tarantula Nebula, binary evolution is required on the basis of BPASS models to match the least luminous WR stars. In addition, BPASS predicts larger stellar number densities for WR stars and luminous blue ($\log L/L_\odot \gtrsim 5.8$) and red supergiants ($\log L/L_\odot \gtrsim 5.3$), which would considerably contribute to the radiative and mechanical output of the Tarantula Nebula. A potential top-heavy IMF would amplify the discrepancy between observation and prediction and has implications for the analysis and interpretation of unresolved stellar populations in star-forming galaxies.

ACKNOWLEDGEMENTS

We thank the referee, Tomer Shenar, for providing helpful comments and suggestions which improved the clarity and content of the manuscript. We thank Chris Evans and Hugues Sana for comments to this manuscript. We would like to thank Nolan Walborn for the spectral classification, which will be published in Paper III. Financial support to Azalee Bostroem from Nolan Walborn's *HST* grant NAS 5-26555 and thanks to Azalee Bostroem for the work on the data reduction. JMB acknowledges financial support from the

Downloaded from https://academic.oup.com/mnras/article/499/2/1918/5905414 by guest on 11 February 2026

University of Sheffield. JMA acknowledges support from the Spanish Government Ministerio de Ciencia e Innovación through grant PGC-2018-095 049-B-C22. SS-D and AHD acknowledge funding from the Spanish Government Ministerio de Ciencia e Innovación through grants PGC-2018-091 3741-B-C22, SEV 2015-0548, and CEX2019-000920-S, and from the Canarian Agency for Research, Innovation and Information Society (ACIISI), of the Canary Islands Government, and the European Regional Development Fund (ERDF), under grant with reference ProID2017010115.

DATA AVAILABILITY

The data underlying this article are available in the article and in its online supplementary material. Reduced spectroscopic data will be published in Paper III.

REFERENCES

Asplund M., Grevesse N., Sauval A. J., 2005, in Barnes T. G., III, Bash F. N., eds, ASP Conf. Ser. Vol. 336, Cosmic Abundances as Records of Stellar Evolution and Nucleosynthesis. Astron. Soc. Pac., San Francisco, p. 25
Banerjee S., Kroupa P., 2012, A&A, 547, A23
Banerjee S., Kroupa P., Oh S., 2012, MNRAS, 426, 1416
Bestenlehner J. M., 2020, MNRAS, 493, 3938
Bestenlehner J. M. et al., 2011, A&A, 530, L14
Bestenlehner J. M. et al., 2014, A&A, 570, A38
Bressert E. et al., 2012, A&A, 542, A49
Britavskiy N. et al., 2019, A&A, 624, A128
Bromm V., Coppi P. S., Larson R. B., 1999, ApJ, 527, L5
Brott I. et al., 2011, A&A, 530, A115
Campbell M. A., Evans C. J., Mackey A. D., Gieles M., Alves J., Ascenso J., Bastian N., Longmore A. J., 2010, MNRAS, 405, 421
Cantiello M. et al., 2009, A&A, 499, 279
Castro N., Crowther P. A., Evans C. J., Mackey J., Castro-Rodriguez N., Vink J. S., Melnick J., Selman F., 2018, A&A, 614, A147
Castro N., Fossati L., Langer N., Simón-Díaz S., Schneider F. R. N., Izzard R. G., 2014, A&A, 570, L13
Chabrier G., 2003, PASP, 115, 763
Cignoni M. et al., 2015, ApJ, 811, 76
Crowther P. A., 2019, Galaxies, 7, 88
Crowther P. A., Dessart L., 1998, MNRAS, 296, 622
Crowther P. A., Schnurr O., Hirschi R., Yusof N., Parker R. J., Goodwin S. P., Kassim H. A., 2010, MNRAS, 408, 731
Crowther P. A. et al., 2016, MNRAS, 458, 624
Davies B., Crowther P. A., Beasor E. R., 2018, MNRAS, 478, 3138
de Koter A., Heap S. R., Hubeny I., 1997, ApJ, 477, 792
de Koter A., Heap S. R., Hubeny I., 1998, ApJ, 509, 879
de Koter A., Schmutz W., Lamers J. G. L. M., 1993, A&A, 277, 561
De Marchi G. et al., 2011, ApJ, 739, 27
Doran E. I. et al., 2013, A&A, 558, A134
Ekström S. et al., 2012, A&A, 537, A146
Eldridge J. J., Stanway E. R., Xiao L., McClelland L. A. S., Taylor G., Ng M., Greis S. M. L., Bray J. C., 2017, Publ. Astron. Soc. Aust., 34, e058
Evans C. J. et al., 2011, A&A, 530, A108
Figer D. F., 2005, Nature, 434, 192
Friend D. B., Castor J. I., 1983, ApJ, 272, 259
Grin N. J. et al., 2017, A&A, 600, A82
Gräfener G., Hamann W.-R., 2008, A&A, 482, 945
Gräfener G., Koesterke L., Hamann W.-R., 2002, A&A, 387, 244
Gräfener G., Vink J. S., de Koter A., Langer N., 2011, A&A, 535, A56
Hainich R. et al., 2014, A&A, 565, A27
Hamann W.-R., Gräfener G., 2004, A&A, 427, 697
Heger A., Woosley S. E., 2002, ApJ, 567, 532
Herrero A., Kudritzki R. P., Vilchez J. M., Kunze D., Butler K., Haser S., 1992, A&A, 261, 209
Herrero A., Lennon D. J., 2004, in Maeder A., Eenens P., eds, Proc. IAU Symp. 215, Stellar Rotation. Kluwer, Dordrecht, p. 209
Higgins E. R., Vink J. S., 2019, A&A, 622, A50
Hillier D. J., Miller D. L., 1998, ApJ, 496, 407
Holgado G. et al., 2018, A&A, 613, A65
Hummer D. G., 1982, ApJ, 257, 724
Hunter D. A., Shaya E. J., Holtzman J. A., Light R. M., O'Neil E. J., Lynds R., 1995, ApJ, 448, 179
Hunter I. et al., 2007, A&A, 466, 277
Hénault-Brunet V. et al., 2012, A&A, 546, A73
Khorrami Z. et al., 2017, A&A, 602, A56
Korn A. J., Keller S. C., Kaufer A., Langer N., Przybilla N., Stahl O., Wolf B., 2002, A&A, 385, 143
Kozyreva A., Yoon S.-C., Langer N., 2014, A&A, 566, A146
Kroupa P., 2001, MNRAS, 322, 231
Krumholz M. R., 2015, Astrophysics and Space Science Library, Vol. 412, The Formation of Very Massive Stars. Springer International Publishing, Switzerland, p. 43
Kudritzki R. P., Cabanne M. L., Husfeld D., Niemela V. S., Groth H. G., Puls J., Herrero A., 1989, A&A, 226, 235
Kudritzki R. P., Lennon D. J., Puls J., 1995, in Walsh J. R., Danziger I. J., eds, Science with the VLT. Springer-Verlag, Berlin, p. 246
Köhler K. et al., 2015, A&A, 573, A71
Langer N., 2009, Nature, 462, 579
Langer N., 2012, ARA&A, 50, 107
Langer N., Norman C. A., de Koter A., Vink J. S., Cantiello M., Yoon S.-C., 2007, A&A, 475, L19
Leitherer C. et al., 1999, ApJS, 123, 3
Lennon D. J. et al., 2018, A&A, 619, A78
Lucy L. B., Abbott D. C., 1993, ApJ, 405, 738
Mahy L., Damerdji Y., Gosset E., Nitschelm C., Eenens P., Sana H., Klotz A., 2017, A&A, 607, A96
Mahy L. et al., 2020, A&A, 634, A118
Markova N., Puls J., Langer N., 2018, A&A, 613, A12
Markova N., Puls J., Repolust T., Markov H., 2004, A&A, 413, 693
Markova N., Puls J., Scuderi S., Markov H., 2005, A&A, 440, 1133
Martins F., Palacios A., 2013, A&A, 560, A16
Martins F., Schaerer D., Hillier D. J., 2005, A&A, 436, 1049
Massey P., Hunter D. A., 1998, ApJ, 493, 180
Massey P., Neugent K. F., Hillier D. J., Puls J., 2013, ApJ, 768, 6
Maíz Apellániz J., 2013, in Guirado J. C., Lara L. M., Quilis V., Gorgas J., eds, Highlights of Spanish Astrophysics VII. p. 583
Maíz Apellániz J. et al., 2014, A&A, 564, A63
Maíz Apellániz J. et al., 2019, A&A, 626, A20
McEvoy C. M. et al., 2015, A&A, 575, A70
Meynet G., Maeder A., Schaller G., Schaerer D., Charbonnel C., 1994, A&AS, 103, 97
Moe M., Di Stefano R., 2017, ApJS, 230, 15
Mokiem M. R. et al., 2007, A&A, 465, 1003
Muijres L. E., Vink J. S., de Koter A., Müller P. E., Langer N., 2012, A&A, 537, A37
Pellegrini E. W., Baldwin J. A., Ferland G. J., 2011, ApJ, 738, 34
Pietrzyński G. et al., 2019, Nature, 567, 200
Prinja R. K., Barlow M. J., Howarth I. D., 1990, ApJ, 361, 607
Puls J., 1987, A&A, 184, 227
Puls J., Urbaneja M. A., Venero R., Repolust T., Springmann U., Jokuthy A., Mokiem M. R., 2005, A&A, 435, 669
Puls J., Vink J. S., Najarro F., 2008, A&AR, 16, 209
Puls J. et al., 1996, A&A, 305, 171
Ramachandran V. et al., 2019, A&A, 625, A104
Ramírez-Agudelo O. H. et al., 2017, A&A, 600, A81
Renzo M. et al., 2019, MNRAS, 482, L102
Rivero González J. G., Puls J., Massey P., Najarro F., 2012b, A&A, 543, A95
Rivero González J. G., Puls J., Najarro F., 2011, A&A, 536, A58
Rivero González J. G., Puls J., Najarro F., Brott I., 2012a, A&A, 537, A79
Sabbi E. et al., 2012, ApJ, 754, L37
Sabín-Sanjulián C. et al., 2014, A&A, 564, A39
Sabín-Sanjulián C. et al., 2017, A&A, 601, A79

Downloaded from https://academic.oup.com/mnras/article/499/2/1918/5905414 by guest on 11 February 2026

Salpeter E. E., 1955, ApJ, 121, 161
Sana H. et al., 2012, Science, 337, 444
Sana H. et al., 2013, A&A, 550, A107
Santolaya-Rey A. E., Puls J., Herrero A., 1997, A&A, 323, 488
Sanyal D., Grassitelli L., Langer N., Bestenlehner J. M., 2015, A&A, 580, A20
Schaerer D., Meynet G., Maeder A., Schaller G., 1993, A&AS, 98, 523
Schmutz W., Hamann W.-R., Wessolowski U., 1989, A&A, 210, 236
Schneider F. R. N., Langer N., de Koter A., Brott I., Izzard R. G., Lau H. H. B., 2014a, A&A, 570, A66
Schneider F. R. N. et al., 2014b, ApJ, 780, 117
Schneider F. R. N. et al., 2018a, Science, 359, 69
Schneider F. R. N. et al., 2018b, A&A, 618, A73
Shenar T., Gilkis A., Vink J. S., Sana H., Sand er A. A. C., 2020, A&A, 634, A79
Shenar T. et al., 2017, A&A, 598, A85
Shenar T. et al., 2019, A&A, 627, A151
Simón-Díaz S., Castro N., Herrero A., Puls J., Garcia M., Sabín-Sanjulián C., 2011, J. Phys.: Conf. Ser., 328, 012021
Simón-Díaz S., Herrero A., 2014, A&A, 562, A135
Stanway E. R., Eldridge J. J., 2018, MNRAS, 479, 75
Stevance H., Eldridge J., Stanway E., 2020, J. Open Source Softw., 5, 1987
Sundqvist J. O., Puls J., 2018, A&A, 619, A59
Tehrani K. A., Crowther P. A., Bestenlehner J. M., Littlefair S. P., Pollock A. M. T., Parker R. J., Schnurr O., 2019, MNRAS, 484, 2692
Vacca W. D., Garmany C. D., Shull J. M., 1996, ApJ, 460, 914
Vink J. S., 2015, Astrophysics and Space Science Library, Vol. 412, Very Massive Stars in the Local Universe. Springer International Publishing, Switzerland
Vink J. S., 2018, A&A, 615, A119
Vink J. S., Brott I., Gräfener G., Langer N., de Koter A., Lennon D. J., 2010, A&A, 512, L7
Vink J. S., de Koter A., Lamers H. J. G. L. M., 2000, A&A, 362, 295
Vink J. S., de Koter A., Lamers H. J. G. L. M., 2001, A&A, 369, 574
Vink J. S., Gräfener G., 2012, ApJ, 751, L34
Vink J. S., Muijres L. E., Anthonisse B., de Koter A., Gräfener G., Langer N., 2011, A&A, 531, A132
Vink J. S. et al., 2015, Highlights Astron., 16, 51
Walborn N. R., 1991, in Haynes R., Milne D., eds, Proc. IAU Symp. 148, The Magellanic Clouds. Kluwer, Dordrecht, p. 145
Yusof N. et al., 2013, MNRAS, 433, 1114

SUPPORTING INFORMATION

Supplementary data are available at *MNRAS* online.

Table S1. Comparison of stellar parameters to previous studies using spectra of spatially resolved stars. Used spectra and wavelength ranges: Massey & Hunter (1998): optical (*HST* /FOS), de Koter et al. (1997, 1998): UV (*HST* /GHRS) + optical (*HST* /FOS), Crowther et al. (2010): UV (*HST* /GHRS), optical (*HST* /FOS) + near-IR (VLT/SINFONI), this study: optical (*HST* /STIS).

Figure S1. Example χ^2 distributions of stellar parameters for a low S/N star. All stellar parameters seemed to be degenerated.
Figure S2. Example χ^2 distributions of stellar parameters for a star hotter than 45 000 K. The temperature has been adjusted based on the N III-IV-V ionization balance.
Figure S3. Evolutionary HRD based on the output of BONNSAI. Stars are preferentially located near the ZAMS.
Figure S4. Example spectroscopic fit of H35. Top panel: red solid line is the model spectral energy distribution. Blue boxes are optical B (F438W), V (F555W) band photometry from De Marchi et al. (2011) and near-IR K_s band photometry from Khorrami et al. (2017). Panel 2 to 4: blue solid line is the observed *HST* spectrum while the red dashed line is the fitted synthetic spectrum.
Figure S5. Spectroscopic fit to the data of R136a5. Blue solid line is the observed *HST* /STIS spectrum. Black dashed line is the synthetic spectrum computed with FASTWIND. Red solid line is the synthetic spectrum computed with CMFGEN. Stellar parameters are given in Table 1.
Figure S6. Spectroscopic fit to the data of R136b. Blue solid line is the observed *HST* /STIS spectrum. Black dashed line is the synthetic spectrum computed with FASTWIND. Red solid line is the synthetic spectrum computed with CMFGEN. Stellar parameters are given in Table 1.
Figure S7. Spectroscopic fit to the data of H36. Blue solid line is the observed *HST* /STIS spectrum. Black dashed line is the synthetic spectrum computed with FASTWIND. Red solid line is the synthetic spectrum computed with CMFGEN. Stellar parameters are given in Table 1.
Figure S8. Observed $\log L$ against predicted by BONNSAI: there is a good agreement between both $\log L$s, but BONNSAI tends to systematically under-predict the observed luminosities. Stars with initial masses $> 40 M_{\odot}$ are shown as blue triangles.
Figure S9. Helium abundances versus initial mass. 1.2 Myr isochrones are overlaid with initial rotation velocities ($v_{\rm rot,ini}$) of 0, 200, 300 and 400 km/s. The He composition of the WNh stars can be reproduced at a similar age by varying $v_{\rm rot,ini}$.
Figure S10. Mass-loss rate over mass versus helium abundance.
Figure S11. Same as Fig. 14 but with an overlaid single star stellar population synthesis.
Figures S12 to S66. Spectroscopic fits to all stars in our sample.

Please note: Oxford University Press is not responsible for the content or functionality of any supporting materials supplied by the authors. Any queries (other than missing material) should be directed to the corresponding author for the article.

This paper has been typeset from a TEX/LATEX file prepared by the author.

Downloaded from https://academic.oup.com/mnras/article/499/2/1918/5905414 by guest on 11 February 2026